

The Globular Cluster Systems of the Early-type Galaxies NGC 3379,
NGC 4406, and NGC 4594
and Implications for Galaxy Formation

Katherine L. Rhode^{1,2}

Department of Astronomy, Yale University, New Haven, CT 06520

rhode@astro.yale.edu

Stephen E. Zepf¹

Department of Physics & Astronomy, Michigan State University, East Lansing, MI 48824

zepf@pa.msu.edu

ABSTRACT

We have investigated the global properties of the globular cluster (GC) systems of three early-type galaxies: the Virgo cluster elliptical NGC 4406, the field elliptical NGC 3379, and the field S0 galaxy NGC 4594. These galaxies were observed as part of a wide-field CCD survey of the GC populations of a large sample of normal galaxies beyond the Local Group. Images obtained with the Mosaic detector on the Kitt Peak 4-m telescope provide radial coverage to at least $24'$, or ~ 70 – 100 kpc. We use *BVR* photometry and image classification to select GC candidates and thereby reduce contamination from non-GCs, and HST WFPC2 data to help quantify the contamination that remains. The GC systems of all three galaxies have color distributions with at least two peaks and show modest negative color gradients. The proportions of blue GCs range from 60–70% of the total populations. The GC specific frequency (S_N) of NGC 4406 is 3.5 ± 0.5 , $\sim 20\%$ lower than past estimates and nearly identical to S_N for the other Virgo cluster elliptical included in our survey, NGC 4472. S_N for NGC 3379 and NGC 4594 are 1.2 ± 0.3 and 2.1 ± 0.3 , respectively; these are similar to past values but the errors have been reduced by a factor of 2–3. We compare our results for the early-type sample (including NGC 4472) to models for the formation of massive galaxies and their GC systems. Of the scenarios we consider, a hierarchical merging picture — in which metal-poor GCs form at high redshift in protogalactic building blocks and metal-rich GC populations are built up over time during subsequent gas-rich mergers — appears most consistent with the data.

¹Visiting Astronomer, Kitt Peak National Observatory, National Optical Astronomy Observatories, which is operated by the Association of Universities for Research in Astronomy (AURA), Inc., under cooperative agreement with the National Science Foundation.

²NASA Graduate Student Researchers Program Fellow

Subject headings: galaxies: individual (NGC 3379, NGC 4406, NGC 4594); galaxies: star clusters; galaxies: elliptical and lenticular, cD; galaxies: formation

1. Introduction

Globular clusters (GCs) are an important constituent of galaxies of all morphological types. Early-type galaxies such as giant ellipticals and cD galaxies have long been known to have very populous GC systems (Baum 1955; Sandage 1961), often consisting of thousands of clusters (Harris 1991; Ashman & Zepf 1998). Much of the work on extragalactic GC systems has focused on understanding how these enormous populations of GCs and their host galaxies formed.

Various models have been proposed that either predict or attempt to explain how it is that ellipticals have such populous GC systems and also that in many cases broadband colors indicate the presence of two or more distinct populations of GCs (e.g., Zepf & Ashman 1993, Geisler, Lee, & Kim 1996, Gebhardt & Kissler-Patig 1999, Larsen et al. 2001, Kundu & Whitmore 2001). For example, Ashman & Zepf (1992; AZ92) suggested that ellipticals are formed when two more disk galaxies merge; GCs in the progenitor spirals make up the metal-poor population of the elliptical, and its metal-rich GCs are formed during the merger itself. Observations of bimodal color distributions in GCs (e.g., Zepf & Ashman 1993) and massive star clusters forming in mergers (e.g., Whitmore et al. 1993; Whitmore & Schweizer 1995) agreed with earlier predictions of AZ92, lending support to the model. Subsequently, other models were proposed to also account for these observations. Forbes, Brodie, & Grillmair (1997a; FBG97) put forth the idea that metal-poor GCs in ellipticals formed during the collapse of a protogalactic gas cloud, and metal-rich GCs originated in a subsequent phase of star formation. Côté, Marzke, & West (1998; CMW98) asserted instead that it is the metal-rich GCs that are formed during the initial collapse, and metal-poor ones are accreted into the elliptical's halo along with the dwarf galaxies that host them. More recently, the idea that galaxies and their globular cluster populations form in galaxy mergers has been put into a cosmological context by Beasley et al. (2002) and Santos (2003). These authors have suggested that metal-poor GCs are formed at high redshift in protogalactic building blocks; in this type of scenario, massive ellipticals and their metal-rich GC subpopulations are built up over time via hierarchical merging.

We initiated a wide-field CCD survey of the GC systems of a sample of massive galaxies with the goal of improving the observational data so that it could begin to distinguish between the various models. In such a photometric survey, the signature of a GC system around a galaxy is an overdensity of compact objects with the colors and magnitudes expected for GCs at that distance. Past surveys were carried out before the advent of wide-field, mosaiced CCD imagers, and typically selected GCs in one or two filters. As a result, the GC candidate samples often were significantly contaminated by foreground stars and background galaxies and many times only a small portion of the GC system was observed (sometimes less than 10%; see Appendix in Ashman & Zepf 1998). Large extrapolations were therefore necessary in order to derive global properties of

the GC systems, such as overall mean colors, total numbers, and specific frequencies, making these values subject to considerable uncertainties. Well-constrained global values are what is needed to test the model predictions as well as to improve our overall understanding of GC systems and their relationship to galaxy formation.

Accordingly, we have observed the GC systems of a large sample of both early-type and spiral galaxies. The survey employs wide-field CCD imaging to observe the full extent of the galaxy GC systems, good resolution to help eliminate background galaxies from the GC candidate lists, and three-color photometry to isolate *bona fide* GCs from contaminating stars and galaxies. In addition, archival Hubble Space Telescope (HST) images are available for most of the targets; these data are used to help quantify the level of contamination in the GC lists.

In Paper I of this series (Rhode & Zepf 2001), we published our results for the giant elliptical NGC 4472, the brightest galaxy in Virgo. We used NGC 4472 as a test case, in order to refine our techniques for finding GCs and removing and quantifying contamination. Paper II (Rhode & Zepf 2003) describes the results for the first spiral to be fully analyzed, NGC 7814. Here we present results for the rest of the early-type galaxy sample: NGC 4406, another giant elliptical in Virgo; NGC 3379, a less-luminous elliptical in the Leo-I group; and NGC 4594, a field galaxy that is intermediate between ellipticals and early-type spirals. Table 1 summarizes the basic properties of the galaxies in the early-type sample, including NGC 4472. We chose galaxies located in different environments and with a range of luminosities in order to investigate how the properties of their GC systems depend on these factors.

The paper is organized as follows: Section 2 summarizes the observations and initial reductions of the data. Section 3 describes our methods for detecting and selecting GC candidates around the target galaxies, as well as our techniques for quantifying how much of the GC system has been observed. Results, including the spatial and color distributions of the GC candidates and the total number and specific frequency of GCs for each galaxy, are presented in Section 4. The last two sections consist of a discussion of the results and their implications for galaxy formation models, followed by a summary of our conclusions.

2. Observations and Initial Reductions

The early-type galaxy sample was imaged in 1999 March with the Mosaic Imager on the 4-m Mayall Telescope at Kitt Peak National Observatory (KPNO). The Mosaic is made up of eight 2048 x 4096 CCDs separated by small gaps ~ 50 pixels wide. It provides a $36' \times 36'$ field-of-view when mounted on the Mayall telescope and each pixel subtends $0.26''$ of sky. Five images were taken through each of three broadband filters (BVR) and the telescope was dithered between exposures to facilitate cosmic ray removal and provide sky coverage in the gaps between the CCDs. Total integration times were 5400s in V and ranged from 3300s to 3900s in B and 2100s to 2400s in R . All the images except the B exposures of NGC 3379 were taken under clear, but not photometric,

conditions. The B observations of NGC 3379 were taken on a subsequent night under poorer sky conditions, resulting in a combined B image that is relatively shallow.

Initial data reduction steps were executed using the IRAF³ package MSCRED. We executed the same steps described in Paper I to process the images (i.e., to perform overscan and bias subtraction and flat-field division) and construct a single, stacked image in each of the three filters for each galaxy. The resolution (point-spread function FWHM) of the final stacked images ranges from 1.0'' to 1.2'' for NGC 4594 and NGC 4406, and from 1.3'' to 1.4'' for NGC 3379.

Because the Mosaic data were taken during nonphotometric conditions, additional calibration data were obtained at KPNO with the WIYN 3.5-m telescope⁴ and Minimosaic camera on photometric nights in 2001 April (for NGC 4406) and 2002 March (for NGC 3379 and NGC 4594). Single short (400–600s) BVR exposures were taken of each galaxy along with several sets of standard star frames (Landolt 1992). The Landolt standards were first used to calibrate the WIYN data. Then ~ 20 bright but unsaturated stars were found in common between the WIYN galaxy images and the stacked Mosaic images. Magnitudes and colors of these stars were measured in both sets of images and photometric coefficients were derived to post-calibrate the Mosaic data to the WIYN data.

3. Data Analysis

Below are outlined the steps used to analyze the GC systems of the three galaxies discussed in this paper; see Paper I for a more detailed description of our methods.

3.1. Source Detection and Matching

To locate GC candidates in the stacked Mosaic images of each galaxy, we smoothed the images with a ring median filter of diameter 6 times the mean FWHM of point sources in the image. Subtracting the smoothed images from the originals removed the galaxy light while preserving the flux from the discrete sources. A constant background level was added to the galaxy-subtracted images and DAOFIND was used to detect all sources above a specified threshold (typically, between three and five times the noise in the local background). A final list of objects appearing in all three filters was produced; the total number of detected sources was 3224 in NGC 3379, 12502 in NGC 4406, and 8053 in NGC 4594.

³IRAF is distributed by the National Optical Astronomy Observatories, which are operated by AURA, under cooperative agreement with the National Science Foundation.

⁴The WIYN Observatory is a joint facility of the University of Wisconsin, Indiana University, Yale University, and the National Optical Astronomy Observatories.

3.2. Extended Source Cut

To eliminate contaminating background galaxies from the source lists, we measured the FWHM and instrumental magnitude of each source. Objects with FWHM values larger or smaller than expected for a point source of a given magnitude were rejected. As an example, FWHM versus magnitude for 8053 sources in the Mosaic V -band image of NGC 4594 is plotted in Figure 1. Open squares are sources deemed extended and filled circles are those that passed the extended source cut. As the figure demonstrates, the range of acceptable FWHM values increases with increasing instrumental magnitude. For NGC 4406 and NGC 4594, we used measurements in all three filters to decide whether a source was extended. The B image of NGC 3379 had poorer resolution so only the V and R images were used. Typically, 30–50% of the objects in the original source lists were removed in this step; the number of accepted sources was 1728 in NGC 3379, 6604 in NGC 4406, and 5708 in NGC 4594.

3.3. Photometry

Photometry with an aperture of radius equal to the average FWHM of the images was performed for objects that passed the extended source cut. Calibrated B , V , and R magnitudes were then computed using the appropriate aperture correction and photometric calibration coefficients. The aperture corrections, which were derived in the same way as for Paper I, are listed in Table 2; the values given are the difference between the total magnitude and that within the small aperture. The final magnitudes were corrected for Galactic extinction using reddening data from Schlegel, Finkbeiner & Davis (1998); the extinction corrections are given in Table 3.

3.4. Color Selection

Observations in three filters can help separate GCs from contaminating background galaxies because in the BVR color-color plane, GCs are well-separated from early-type spirals and ellipticals and high-redshift galaxies. They overlap low-redshift, late-type spirals and moderate-redshift irregulars, but many of the low- z objects are eliminated in the extended source cut. Thus combining three-filter photometry with image analysis substantially reduces the level of contamination in our GC candidate lists.

The color selection was executed as follows: objects with absolute magnitude brighter than $M_V = -11$ (assuming the galaxy distances listed in Table 1) were eliminated. A photometric error threshold of 0.125 to 0.15 magnitudes in one or more filters (depending on the quality of the images) was also imposed. Finally, taking into account their photometric errors, objects with $B - V$ between 0.56 and 0.99 (corresponding to $[\text{Fe}/\text{H}]$ of -2.5 to 0.0 for Galactic GCs) and $V - R$ values that put them within a specified distance from the relation between $B - V$ and $V - R$ for Galactic

GCs were retained. The distance from the $B - V$ versus $V - R$ line that was deemed acceptable varied. For NGC 4406 and NGC 4594, the data were of good quality and a $2-\sigma$ distance above and below the line (where σ is the scatter in the relation for Milky Way GCs) was sufficient. The B image of the NGC 3379 field was very shallow and the detected sources were preferentially blue; for this reason we accepted objects that were within $1-\sigma$ above the line (redder than Milky Way GCs) and $3-\sigma$ below it (bluer than Milky Way GCs).

Two of the galaxies in the early-type sample have companion galaxies that appear in the Mosaic images. NGC 3384 is an SB0 galaxy in the Leo group and is located only $7'$ (22 kpc in projection) away from NGC 3379. NGC 4374, a Virgo cluster E1 with $M_V = -22.05$, is situated $\sim 17'$ (75 kpc in projection) west of NGC 4406. In both cases these galaxies' GC systems were readily apparent in the images as surrounding overdensities of point sources with GC-like colors. In order to eliminate these objects from the final lists of GC candidates, we marked a region around the companion galaxies and removed any source located within that region. These areas were also excluded from the spatial coverage calculation described in Section 4.1.

The final lists of GC candidates around NGC 3379, NGC 4406, and NGC 4594 contained 321, 1400, and 1748 objects, respectively. Figures 2 through 4 show the results of the color selection. The locations in the BVR color-color plane of sources that passed the extended source cut are shown as open squares, and the GC candidates are plotted as filled circles.

3.5. Completeness Testing

To quantify the detection limits of the Mosaic images, a series of completeness tests was executed for each galaxy. First, 800 artificial point sources with magnitudes within 0.2-mag of a specified mean value were added to the B , V , and R images. Then the same detection steps executed on the original images were performed and the fraction of artificial stars recovered in the detection process was recorded. The process was repeated over a range of 3–5 magnitudes for each filter. The 50% completeness limits are listed in Table 4. As mentioned earlier, the B image of NGC 3379 was taken under poor sky conditions and is relatively shallow. Consequently the B detection limit dominates the completeness corrections and the fractional GCLF coverage calculated in Section 3.7 is smaller than intended, despite NGC 3379's relative proximity.

3.6. Quantifying and Correcting for Contamination

3.6.1. Galaxies

Compact galaxies that appear as point sources in ground-based data are often resolved in images taken with the Wide-Field and Planetary Camera 2 (WFPC2) on HST. Therefore by locating a subset of our GC candidates in archival WFPC2 images and determining how many are galaxies,

we can estimate the level of galaxy contamination that exists in the data.

WFPC2 observations in broadband filters of fields within $15'$ of the centers of NGC 3379, NGC 4406, and NGC 4594 were retrieved from the HST archive⁵. “On-the-fly” calibration was applied to the images. Table 5 summarizes the data sets we analyzed. Column (1) gives HST proposal ID; column (2) is the target name (names like “Parallel Field” and “Any” are observations done by WFPC2 while another instrument was being used for the primary science); column (3) is the Principal Investigator; column (4) is the angular separation of the pointing from the center of the target galaxy; and column (5) is the filter. When possible, combined images were created with the STSDAS task CRREJ. WCSTRAN was used to locate the Mosaic GC candidates in the WFPC2 frames. Following the method of Kundu et al. (1999), we measured the flux of the candidates in two apertures to decide which were galaxies. Kundu et al. found that at the distance of Virgo, objects in a WF chip with $\text{counts}_{3pix}/\text{counts}_{0.5pix} > 8$ are extended. (None of our GC candidates appeared in the PC chip.) This criterion was used for the NGC 4406 data. For NGC 3379 and NGC 4594, we determined that sources with count ratios > 10 and 12 , respectively, were galaxies. We also visually inspected the GC candidates to confirm the results from photometry.

The final statistics are as follows: one of 23 GC candidates appearing in the WFPC2 images of NGC 3379 is a galaxy; two of 57 GC candidates in NGC 4406 are galaxies; and five of 43 GC candidates in NGC 4594 are galaxies. Combining the number of galaxies with the usable area covered by the WFPC2 frames yields the estimated number density of galaxies in our samples. The number densities for NGC 3379, NGC 4406 and NGC 4594 are, respectively, 0.08 per square arc minute, 0.16 per square arc minute, and 0.26 per square arc minute.

3.6.2. Stars

We ran the Galactic structure model code from Mendez & van Altena (1996) and Mendez et al. (2000) to estimate how many foreground stars are included in the GC candidate lists. Given values for parameters such as the solar distance and the proportion of stars in the various components of the Galaxy, the model calculates the surface density of Galactic stars in a given magnitude and color range in a specific direction on the sky. The model predicts that in the direction of NGC 3379, the number density of stars with V magnitudes and $B - V$ colors in the same range as the GC candidates is 0.11 per square arc minute. The answer was the same for NGC 4406. For NGC 4594, the stellar surface density was 0.28 per square arc minute. The results were relatively insensitive to changes in our choice of the composition of the Milky Way and the location of the Sun within the disk.

⁵Based on observations made with the NASA/ESA *Hubble Space Telescope*, obtained from the data archive at the Space Telescope Science Institute. STScI is operated by AURA, under NASA contract NAS 5-26555.

3.6.3. Radially-Dependent Contamination Correction

The estimated fraction of contaminating objects at each radius around the target galaxies was calculated for use in subsequent steps. The GC candidates in each galaxy were assigned to annuli of width $1'$, with the first annulus centered at $r \sim 1'$ and the last at $r \sim 24'$ for NGC 3379 and NGC 4406, and at $r \sim 25'$ for NGC 4594. The number of contaminating objects in each annulus was calculated by multiplying the number density of stars plus galaxies by the effective area (the region in which GCs could actually be detected; see Section 4.1) of the annulus. Dividing the number of contaminating objects by the number of GC candidates in each annulus yielded the contamination fraction as a function of radius. NGC 4594 and NGC 4406 have large numbers of GC candidates so the contamination fraction is modest at radii inside 7–10' (e.g., in NGC 4406 it is 20% by 10', or ~ 45 kpc). The GC system of NGC 3379 is more sparsely populated, so the estimated contamination fraction climbs quickly in the inner few arc minutes, already reaching $\sim 40\%$ by 4' (~ 12 kpc).

3.7. Determining the GCLF Coverage

An observed GC luminosity function (GCLF) for each galaxy was constructed by assigning the V magnitudes of the GC candidates to bins of width 0.3 mag. The radially-dependent contamination correction was applied during the binning process. The luminosity function was corrected for completeness by computing the total completeness of each V bin (which involves convolving the completenesses of all three filters, as described in Paper I) and dividing the number of GCs in the bin by this value.

We assumed that the intrinsic GCLFs of the three early-type galaxies had peaks at $M_V = -7.4$, which is consistent with results from HST studies of ellipticals (Kundu & Whitmore 2001). Combining this with the distance moduli listed in Table 1 gives $V = 22.7, 23.7$ and 22.6 for the peak apparent magnitude of the GCLF for NGC 3379, NGC 4406 and NGC 4594, respectively. We constructed Gaussian distributions with these peak magnitudes and dispersions of 1.2, 1.3 and 1.4 mag and fitted them to the observed luminosity functions, varying the normalization of the Gaussian. Bins with less than 45% completeness were excluded from the fits. The fraction of the best-fit theoretical GCLF covered by our data was calculated for each case.

The quality and depth of the observed LF data vary for the three galaxies. For NGC 3379, the data do not reach the turnover of the assumed GCLF and several of the histogram bins are sparsely populated. Different dispersions produced similar-quality fits. The mean fractional coverage derived from all three fits is 0.46 ± 0.01 . The NGC 4406 data also do not reach the peak of the GCLF, but the bins leading up to it are well-populated. The Gaussian with 1.4-mag dispersion clearly yielded the best fit; the associated fractional coverage is 0.51. (Smaller dispersions produced values within 1% of this.) For NGC 4594, the observed data go well past the peak of the GCLF and are well-fit by a Gaussian with 1.4-mag dispersion and inconsistent with smaller dispersions. The fractional

coverage is 0.83. Figure 5 shows the GCLF fits for the three galaxies. The shaded histogram is the observed data; the dashed histogram has been corrected for completeness; and the dotted lines are the fitted Gaussian distributions with the lowest χ^2 values.

We investigated whether changes in the bin size of the LF data affected the fractional coverage results for each galaxy. For NGC 3379 and NGC 4406, changing the bin size changed the fractional coverage by as much as 2.5%. For NGC 4594, the observed data covered so much of the GCLF that the change was only a few tenths of a percent. These uncertainties are taken into account in the error calculation in Section 4.4.

4. Results

4.1. Radial Distributions

To investigate the spatial distribution of the GC systems, GC candidates were assigned to $1'$ -wide annuli based on their projected radial distances from the galaxy centers. An effective area was calculated for each annulus that excluded regions where GCs could not be detected (i.e., regions around bright stars and companion galaxies that had been masked out, the central $\sim 0.5'$ of each galaxy, and parts of the annulus that extended off the image). The number of GCs in each annulus was corrected for contamination and GCLF coverage. The corrected radial distributions are shown in Figures 6 through 8 and the numerical values are listed in Table 6. Column (1) of the table gives the mean radius of the unmasked pixels in each annulus, column (2) lists the surface density and associated error, and column (3) gives the fraction of the annulus with spatial coverage.

Each GC profile is different, but in all three cases the surface density decreases until it is consistent with zero in several adjacent bins, well before the end of the data. This suggests that we have observed the full radial extent of the galaxies' GC systems. NGC 3379 has the least populous GC system and the surface density is consistent with zero within the $1\text{-}\sigma$ error bars by the $11'$ bin (~ 30 kpc) and beyond. (It becomes slightly positive in one outer bin at $21'$, but returns to zero or negative values in the next three annuli.) In NGC 4406, the surface density is consistent with zero by $17'$ (~ 75 kpc) outward. NGC 4594's GC surface density decreases to very low values by $15'$ and is zero within the errors in every bin from $19'$ (~ 50 kpc) to the end of the data at $25'$. The innermost point in the radial profile for NGC 4594 has comparatively large error bars because nearly the entire annulus was masked out due to the galaxy's dust lane. Only two GCs were detected in the small region left unmasked. We have included the point in the figure and table for the sake of completeness, but removing it does not change the results.

We fitted the GC spatial distributions with deVaucouleurs law profiles of the form $\log \sigma_{\text{GC}} = a0 + a1 r^{1/4}$ and power laws of the form $\log \sigma_{\text{GC}} = a0 + a1 \log r$; the results are given in Table 7. For NGC 4594 and NGC 4406, the deVaucouleurs law provides a better fit than the power law at large radius, where the data begin to drop slightly or significantly below the best-fit lines. This is

similar to NGC 4472, for which a deVaucouleurs law also fits the GC radial profile better than a power law. For NGC 3379, both the power law and deVaucouleurs law provide good fits out to the limit of the data; the best-fit lines intersect nearly all the points plus error bars. For consistency, we have shown the deVaucouleurs law fits in the figures for all three galaxies (including NGC 3379) and we use them to calculate the total number of GCs for each galaxy in Section 4.4.

The behavior of NGC 4406’s radial distribution is somewhat different from that of the other two galaxies. The data for NGC 3379 and NGC 4594 scatter around the best-fit deVaucouleurs law profile out to the point at which the surface density becomes consistent with zero (marked with a vertical line in the figures), and intersects the error bars of each point in most of the bins inside that line. For NGC 4406, however, the data start to fall below the best-fit line around 10–11’, and by 12’ (~ 50 kpc) onward, they lie systematically below the line. This is not necessarily unexpected behavior (since there is no reason to assume that a deVaucouleurs law *must* provide a good fit over the entire extent of a GC system) but is worth noting in contrast to the other galaxies. NGC 4406 is in a richer environment than NGC 3379 and NGC 4594 and has a massive, close companion; it is perhaps possible that its GC system is showing signs of tidal truncation either due to interaction with NGC 4374 or the tidal field of the Virgo cluster.

Although we had masked out NGC 4374 and its GC system when constructing the radial profile for NGC 4406, we wanted to confirm that the observed behavior of the profile was real and not due to the presence of GCs from NGC 4374 artificially inflating the surface density in the inner few arc minutes. (The masked region begins in the 10’ bin, near where the data start to fall below the best-fit line.) To test this we constructed a radial profile for NGC 4406 using only the side of the galaxy away from NGC 4374, i.e., the eastern half of NGC 4406’s GC system. The extent of this profile is similar to that of the original one; the surface density in the eastern profile is consistent with zero by 15’ outward, whereas the original profile has a slightly positive surface density (0.28 ± 0.27 per square arc minute) in the 16’ bin and then is consistent with zero at larger radius. The slope and intercept of the best-fit deVaucouleurs law are the same for both profiles. Furthermore, the behavior of the eastern-half profile is similar to that of the original profile: the data plus error bars once again fall systematically below the best-fit line from 12’ onward. Therefore it appears that the behavior seen in the original profile is a real effect and not simply due to inadequate masking of NGC 4374’s GC system.

4.2. Color Distributions

To investigate the colors of the GCs in each galaxy, we selected GC candidate samples that are at least 90% complete in all three filters. For example, the reddest GC candidate in NGC 3379 has $B - R = 1.8$ and our detection is 90% complete at $B = 22.5$, so candidates with R brighter than 20.7 were chosen. Any GC candidates found to be galaxies in the HST images were excluded. We also imposed a radial cut at the location where the GC surface density in the radial profile became consistent with zero. This yielded samples of 36, 979, and 1084 objects in NGC 3379, NGC 4406,

and NGC 4594, respectively.

$B - R$ histograms for the early-type galaxy sample are shown in Figure 9, including that for NGC 4472 from Paper I. NGC 4472 has a bimodal distribution with peaks at $B - R \sim 1.1$ and 1.4 and a gap around 1.2; roughly 60% of the GCs are in the blue peak and 40% are red. The data for NGC 4406 show an obvious peak at $B - R \sim 1.1$ and a tail of red GCs, with perhaps hints of secondary peaks around 1.3 and 1.4. NGC 4594’s distribution is wide and, like NGC 4472’s, roughly resembles two overlapping Gaussians. With only 36 GCs included, NGC 3379’s color distribution is too sparse to show clear peaks, but does not appear consistent with a single Gaussian.

We ran the KMM algorithm (Ashman, Bird, & Zepf 1994) on the color distributions, which tests whether a single or multiple Gaussian functions provide a better fit to a distribution. The user specifies the number of Gaussians to fit as well as whether to use the same or different dispersions for each one. The results for each galaxy are as follows:

NGC 3379. KMM requires at least 50 objects to produce a reliable result, so the 36-object sample shown in Figure 9 is too small. Instead we created a sample with exactly 50 objects by taking the 90% sample and imposing a slightly relaxed radial cut — i.e., including objects with radii inside $13.5'$, instead of the $11'$ criterion used to create the 36-object sample. This 50-object sample was used as input to KMM. The unimodal hypothesis was rejected for this sample at 99.8% confidence and peaks were located at $B - R \sim 1.1$ and 1.5. The separation between the two components of the fitted distribution was around $B - R$ of 1.3. If we split the final 36-object color sample at $B - R = 1.3$, we find that 70% of the GC candidates are bluer than this color and 30% are redder. (Note that the color distributions of both the 36-object and 50-object samples are shown in Figure 9.)

NGC 4406. Fitting with two Gaussians yielded peaks at $B - R \sim 1.1$ and 1.4. The proportion of blue GCs was 56% if we chose varying dispersions and 75% if we required them to be the same. Since NGC 4406’s color distribution may show more than two peaks, we also fitted it with three Gaussians. Peaks were located at $B - R \sim 1.1$, 1.3, and 1.5. Between 56 and 58 percent of the GCs were assigned to the first (blue) peak and the remainder to the second two peaks. In every case, the distribution was found to be multimodal at 99.99% confidence. The separation between the GC candidates in the bluest peak and those in the redder peak (or peaks) occurred around $B - R$ of 1.2–1.3.

NGC 4594. The single-Gaussian hypothesis was rejected with 99.99% confidence and a fit with two Gaussians produced peaks at $B - R \sim 1.1$ and 1.5. For Gaussians with identical dispersions, 66% of the GCs were blue; if the dispersions varied, the proportion was 59%. The separation between the blue and red populations occurs at $B - R \sim 1.3$.

NGC 4472, NGC 4406, and NGC 4594 have similar proportions of blue GCs ($\sim 60\%$) whereas NGC 3379 appears to have a slightly larger blue population ($\sim 70\%$ of the total). Preliminary results from a wide-field, ground-based BVR study of NGC 3379’s GC system by Butterworth & Hanes also indicate an excess of blue GC candidates (D. Hanes, private communication). However, the $V - I$ distribution of the inner $0.5'$ of NGC 3379’s GC system from the HST study of Kundu

& Whitmore (2001) appears fairly evenly distributed over the range of $V - I$ colors. In the next section we show that there may be a color gradient in NGC 3379’s GC system in the sense that the ratio of blue to red GCs increases with radius. In this case it might make sense that the HST data in the inner region do not show an excess of blue clusters but that the wide-field data do. If the gradient and the excess of blue GCs in NGC 3379 are real, they underscore the importance of obtaining wide-field data to deriving accurate total numbers of red and blue GCs for comparison to galaxy formation models (see Section 5).

4.3. Color Gradients

A straightforward way to look for color gradients in each galaxy’s GC system is to plot color versus projected radius for a complete sample of GC candidates. Accordingly, Figures 10 through 12 show $B - R$ versus radius for the 90% samples. We fitted lines to the data for each galaxy, imposing the same radial cut that was used to create the input for KMM. The best-fit lines are shown in the figures. To calculate metallicity gradients, we converted the $B - R$ values to $[\text{Fe}/\text{H}]$ (using the relationship derived in Paper I) and fitted lines to $[\text{Fe}/\text{H}]$ versus $\log r$.

All three galaxies show evidence for modest negative color gradients in their overall GC populations. For NGC 4406 and NGC 4594, the slopes of the best-fit lines in the color-radius plane are $\Delta(B - R)/\Delta r = -0.004 \pm 0.001$ and -0.003 ± 0.001 , respectively. These translate to metallicity gradients of $\Delta[\text{Fe}/\text{H}]/\Delta \log r = -0.16 \pm 0.06$ and -0.19 ± 0.06 . NGC 3379 has a formally steeper gradient, but at a lower significance: $\Delta(B - R)/\Delta r = -0.023 \pm 0.010$. The fit includes only 36 points and the scatter is large, so the gradient is significant only at the $2\text{-}\sigma$ level. If we remove the single red GC candidate in NGC 3379 between $7'$ and $11'$, the $B - R$ gradient becomes -0.028 ± 0.010 . Fitting metallicity versus the log of the radius for the full ($N=36$) sample produces $\Delta[\text{Fe}/\text{H}]/\Delta \log r = -0.60 \pm 0.31$.

Two of the galaxies have had the color gradients of their GC systems measured previously. Cohen (1988) studied the inner $\sim 7'$ (~ 30 kpc) of NGC 4406’s GC population with a small-format CCD detector and *gri* filters, and found no detectable color gradient in this region. Our data are consistent with this result: we find $\Delta(B - R)/\Delta r = -0.004 \pm 0.004$ inside $7'$. Bridges & Hanes (1992) observed the inner portion of NGC 4594’s GC system with a small-format CCD and B and V filters. They found no evidence for a gradient in $B - V$ with galactocentric radius for GCs in the inner $\sim 4'$ of the galaxy. We likewise do not find a significant color gradient in our data for this inner region. In a later study, Forbes, Grillmair, & Smith (1997b) observed NGC 4594 over a larger radial range. Using a CCD with $1.84''$ -pixels and B and I filters, they found no color gradient in a sample of ~ 400 GC candidates over the radial range 4–50 kpc. The very coarse resolution of their study (with a pixel scale ~ 7 times larger than the current work) may have resulted in significant contamination from background galaxies, which would affect their ability to detect a gradient.

A cautionary note is that although we have carefully minimized contamination in the GC

samples through multi-color selection and image analysis, the proportion of GCs relative to contaminating objects inevitably decreases with increasing radius. The gradients we find may be affected by this if the contaminating objects are strongly biased in color relative to the GCs. To investigate this possibility, we examined the $B - R$ color distributions of the GC candidates with radial distances beyond the apparent extent of the each galaxies' GC system. In NGC 4594 and NGC 3379, the blue and red proportions of these likely contaminants are very similar to the proportions we derived for the GC systems. In NGC 4406, the contaminants are uniformly distributed in $B - R$. What this indicates is that the contaminating objects are not likely to be heavily biased toward the blue or red with respect to the GCs, which seems to suggest that our overall results for the color gradients are valid.

4.4. Total Numbers and Specific Frequencies

The total number of GCs in the three target galaxies can be calculated by integrating the best-fit deVaucouleurs profile from $r = 0$ to a specified outer radius. We have chosen to stop the integration for each galaxy at the point at which the GC surface density becomes consistent with zero and remains so until the end of the data. As discussed in Section 4.1 this occurs at $11'$, $17'$ and $19'$ for NGC 3379, NGC 4406, and NGC 4594, respectively. To facilitate comparison between galaxies, the total number of GCs (N_{GC}) can be normalized by the galaxy luminosity or mass; the luminosity-normalized specific frequency, S_N , is defined as

$$S_N \equiv N_{GC} 10^{+0.4(M_V + 15)} \quad (1)$$

(Harris & van den Bergh 1981) and the mass-normalized number of GCs, T , is

$$T \equiv \frac{N_{GC}}{M_G / 10^9 M_\odot} \quad (2)$$

(Zepf & Ashman 1993), where M_G is the stellar mass of the host galaxy. Table 8 lists the total numbers and specific frequencies derived for the three target galaxies. Note that to calculate T , we have assumed mass-to-light ratios (M/L_V) of 10 for the two ellipticals and $M/L_V = 7.6$ for the S0 NGC 4594, following Zepf & Ashman (1993). Table 8 also includes the radial extent of each GC system (derived by converting the integration limit used to calculate S_N into a physical distance) along with a list of S_N values from previous studies. Note that to allow straightforward comparison between our S_N values and others', we have normalized N_{GC} from the previous studies with the same M_V values as used in this work; thus any differences in S_N reflect differences in total numbers rather than in host galaxy magnitude or distance.

To estimate the error associated with our S_N values, we calculated the Poisson errors on the total numbers of GCs and contaminating objects, uncertainties related to fitting the GCLF, and uncertainty in the total magnitude of the galaxy. For the latter, we assumed that the galaxy magnitudes could be brighter or fainter by as much as three times the error on V_T^0 given in RC3 (de

Vaucouleurs et al. 1991). We added each of these uncertainties in quadrature to produce an initial estimate of the error. Next, we investigated how the choice of outer integration limit for the radial profile affects S_N . In each galaxy’s radial distribution, the GC surface density becomes negative in one or more of the outer annuli. For this test, we calculated new S_N values by integrating the best-fit deVaucouleurs profiles out to the last bin before σ_{GC} becomes negative. For NGC 4406 and NGC 4594, the integration limit became $21'$ and $22'$, respectively. NGC 3379’s profile is somewhat noisier and σ_{GC} is negative by $11'$, which is where we had originally stopped the integration. In this case we continued the integration to $15'$, since σ_{GC} is negative in the next two annuli after that. The new S_N values for NGC 4406 and NGC 4594 matched the original values within our estimated errors. S_N for NGC 3379 increased by 0.27, whereas we had estimated an initial error of 0.2; to account for this, the final S_N for NGC 3379 is listed in Table 8 as 1.2 ± 0.3 .

As a last check on the derived S_N values, we investigated whether summing the actual data points in the radial distributions rather than integrating the fitted profiles produces S_N values consistent with the final values and errors. For NGC 3379 and NGC 4594, S_N from summing the data matched the values in Table 8. Because NGC 4406’s GC distribution drops below the deVaucouleurs law well before the chosen integration limit, S_N from summing the points is 0.1 smaller than the lower limit given in the table.

4.5. Mass-Normalized Number of Blue Globular Clusters

The relative numbers of blue, metal-poor GCs in the massive ellipticals and spirals we have targeted are especially relevant to the question of how such galaxies formed. The AZ92 merger model, for example, predicts that spirals and ellipticals should have similar numbers of metal-poor GCs, since in their scenario, the metal-poor GC populations in ellipticals come directly from the progenitor spirals. In hierarchical structure formation scenarios like that of Santos (2003), in which metal-poor GC formation occurs over a finite period in the early Universe, massive galaxies in dense environments naturally have larger proportions of metal-poor GCs than lower-mass field galaxies. Accurate determinations of how many blue, metal-poor GCs exist around a given galaxy are therefore important for testing the predictions and assumptions of these models.

Section 4.2 described how KMM was used to estimate the proportion of blue GCs in the three target galaxies. For NGC 3379, we estimated that $\sim 70\%$ of the GC population is blue. For the other two galaxies, the proportion varied by a few percent depending on the conditions used to fit the data with KMM, so we have taken the average of the results as the final value. For NGC 4406, the fraction is .62 and for NGC 4594 it is .63. Combining these values with the number of GCs normalized by galaxy mass yields T_{blue} for each galaxy; the results are listed in column 7 of Table 8.

5. Discussion

The main result of this paper is that by utilizing wide-field CCD detectors and techniques to both reduce and quantify contamination from non-GCs, we have been able to derive robust global values for the GC system properties of the early-type galaxies NGC 3379, NGC 4406, and NGC 4594. Here we discuss our findings as well as examine their implications for the formation of galaxies and their GC populations. As explained in the Introduction, several models for the formation of early-type galaxies and their GC systems have been proposed; these include spiral-spiral mergers (AZ92), multiple phases of star formation (FBG97), dissipational collapse with accretion (CMW98), and hierarchical merging (e.g., Beasley et al. 2002, Santos 2003).

Global specific frequency.— Table 8 shows that the S_N value of the giant elliptical NGC 4406 is reduced by $\sim 20\%$ compared to previous values. The S_N value for the Virgo elliptical NGC 4472 (from Paper I) is also $\sim 20\%$ smaller compared to past work. Both values agree with the previous determinations within their quoted errors, which were about twice as large as ours. The S_N values for NGC 3379 and NGC 4594 are nearly identical to the values found in past studies, but their uncertainties have been reduced to one-third to one-half their former size.

The previous determinations of S_N for NGC 4406 and NGC 4472 were done using photographic plates and it is possible that the numbers were undercorrected for contamination. The power-law profile fits that were typically used to calculate total numbers may have also contributed to the discrepancy with our values. These galaxies' GC systems are more extended than those of the less luminous galaxies in the sample, so overestimating the GC counts at large radius has more of an effect because the summation to derive N_{GC} is done over a larger area.

An interesting and potentially meaningful result is that (despite S_N and its uncertainties having been reduced) the two giant cluster ellipticals in our sample still match closely in terms of the number of GCs per unit luminosity or mass. Their T_{blue} values are also similar. NGC 3379 has $S_N \sim 1$, the lowest value in the early-type sample. This is comparable to S_N for spirals of similar luminosity (see Paper II). NGC 4594's S_N value is midway between that of the cluster ellipticals and spirals, which perhaps makes sense since morphologically, it falls somewhere between spirals and ellipticals. On the other hand, NGC 4594 is a luminous galaxy and has an absolute magnitude like that of NGC 4406. When examined as a whole, the results from the early-type galaxy sample suggest that S_N is dependent at least in part on luminosity/mass of the host galaxy, with possible additional effects from morphology and/or environment.

Specific frequency of blue GCs.— As noted above, the mass-normalized numbers of blue GCs (T_{blue}) for the two luminous Virgo cluster ellipticals in the sample are essentially the same, at 2.6 for NGC 4472 and 2.5 for NGC 4406. NGC 4594, which is of similar luminosity to NGC 4406 and is an early-type field galaxy, has $T_{\text{blue}} = 2.0$. The moderate-luminosity field elliptical NGC 3379 has the smallest T_{blue} of the sample, 1.0.

In Paper II, we estimated T_{blue} for the Sab spiral NGC 7814, a field galaxy with $M_V^T = -20.4$.

Its T_{blue} value is in the range 1–2, so somewhere between that of NGC 3379 and NGC 4594. The Milky Way and M31 have absolute V magnitudes of -21.3 and -21.8 and $T_{\text{blue}} \sim 0.9$ and 1.2 , respectively (see discussion in Paper II). The T_{blue} values of these spirals (all of them located in low-density environments) are on the whole comparable to that of NGC 3379, and smaller than T_{blue} for the giant cluster Es.

The above comparison, taken at face value, suggests that it is unlikely that luminous cluster ellipticals like NGC 4406 and NGC 4472 could have formed from the merger of spirals like the Milky Way, M31, or NGC 7814 in the way that AZ92 envisioned. There do not appear to be enough blue, metal-poor GCs in typical spirals that we see today (assuming the three we are using as examples are typical) to account for the large metal-poor populations of GCs in luminous, high- S_N ellipticals. It *does* seem possible, however, that the blue GC population in a more moderate-luminosity elliptical like NGC 3379 could have come from the merger of spirals like the Milky Way and NGC 7814, since T_{blue} for these galaxies is similar. T_{blue} for NGC 4594 is larger than that for the Galaxy and M31 but falls at the high end of the range we estimate for NGC 7814, so we cannot rule out that an AZ92-like merger could account for its metal-poor GC system.

It is relevant to note again at this point that when calculating T for a given galaxy, one adopts a mass-to-light ratio to convert M_V to total stellar mass. Following the convention set in the paper that introduced the T parameter (Zepf & Ashman 1993), we used the same M/L_V for all three ellipticals. In fact, elliptical galaxy mass-to-light ratios almost certainly vary with luminosity. The simplest reason for this is that elliptical galaxies follow a color-magnitude relation. More luminous ellipticals are redder, and these redder stellar populations are associated with slightly higher M/L_V . Assuming that the color-magnitude relationship is caused by metallicity effects leads to $M/L_V \propto L^{0.07}$ (Dressler et al. 1987), whereas assuming that age is the primary contributor yields a slightly larger exponent (~ 0.10 ; see, e.g., Zepf & Silk 1996). A steeper dependence of M/L_V on L is suggested by studies of the fundamental plane (e.g., Dressler et al. 1987; Faber et al. 1987; Kormendy & Djorgovski 1989). However, this difference is typically ascribed to systematic breaking of the assumption of homology along the elliptical galaxy sequence, or by a larger dark matter contribution in more luminous ellipticals (see, e.g., Pahre, Djorgovski, & de Carvalho 1995 and references therein). Neither of these effects reflect differences in stellar mass-to-light ratios, so the appropriate relation to use to examine the effect of changing M/L_V on our results is that from the stellar populations differences, $M/L_V \propto L^{0.10}$.

Taking into account that the mass-to-light ratios of ellipticals may vary as $L^{0.10}$ reduces the T_{blue} values for the more luminous ellipticals, NGC 4406 and NGC 4472, by a factor of 1.1–1.2 relative to the value for NGC 3379. Our observed values of T_{blue} for NGC 4472 and NGC 4406 are 2.5 times that for NGC 3379, and ~ 2 times larger than the mean T_{blue} value for the three spirals mentioned above. Therefore (as we noted in Paper II), using variable instead of constant mass-to-light ratios accounts for only half or less of the apparent difference in T_{blue} for ellipticals of different luminosity. Thus the differences in T_{blue} between the luminous ellipticals and the less luminous galaxies in the sample appear to be real.

An assumption we make when comparing T_{blue} for spirals and ellipticals *at the present day* is that dynamical destruction has not substantially changed the numbers of metal-poor GCs since the time that the spiral-spiral mergers might have occurred, or that it has had a fairly equal effect on the halo GC populations in both types of galaxies. As we discussed in Paper II, it is possible that this assumption is incorrect and that more GC destruction may have taken place in lower-luminosity ellipticals and spirals compared to high-luminosity ellipticals. If this is the case, it could potentially explain the observed differences in T_{blue} for typical-luminosity ellipticals and spirals versus high-luminosity ellipticals. Avenues for further work in this area include developing new observational tests of the role of dynamical destruction, as well as modeling GC destruction in galaxies with a wider range of properties (e.g., spirals of varying luminosity).

In Paper II we also discussed the idea that hierarchical merging scenarios for the origins of spirals and ellipticals may be able to explain the variation of T_{blue} with galaxy luminosity and environment. In this type of picture, metal-poor GC formation occurs at high redshift in protogalactic fragments or “building blocks” that merge to form larger structures. In the Santos (2003) hierarchical model, GC and structure formation are temporarily suppressed when reionization occurs. The protogalactic fragments in higher-density regions (e.g., in locations that eventually become galaxy clusters) collapse and begin forming metal-poor GCs earlier than those located in lower-density regions. As a result, massive galaxies in high-density environments (like giant cluster ellipticals) have the largest numbers of metal-poor GCs per unit luminosity or mass. Less massive galaxies in poorer environments (like spirals and ellipticals in the field) naturally have smaller T_{blue} values. To complete the scenario, stellar evolution enriches the intergalactic medium during the interval when GC formation is suppressed, so that GCs formed after this interval are comparatively metal-rich. Gaseous merging and hierarchical assembly continue, triggering additional metal-rich GC formation and eventually resulting in massive galaxies that have GC systems with both metal-poor and metal-rich subpopulations. Hierarchical merging — with GC formation being temporarily suppressed (perhaps by reionization) — thus seems to provide a sensible overall framework with which to understand the observation that T_{blue} is apparently larger for the luminous cluster ellipticals and smaller for the field galaxies in the survey.

Color distributions.— The $B - R$ color distributions for the galaxies in the early-type sample are better fit by two Gaussians than a single one at 99.8% confidence or higher. (The distribution for NGC 4406 may actually show hints of three peaks.) The blue peaks of the color distributions are centered at $B - R \sim 1.1$, perhaps suggesting a similar origin for the metal-poor GC populations. The locations of the red (metal-rich) peaks vary slightly, ranging from $B - R \sim 1.3$ to 1.5. The global ratios of red to blue GCs in the two Virgo ellipticals and NGC 4594 are roughly similar, at ~ 0.60 – 0.66 . NGC 3379 appears to have a larger proportion of blue GCs and its red-to-blue ratio is ~ 0.40 .

Different models produce different expectations for the proportions of red and blue GCs in elliptical systems. CMW98 state that giant ellipticals with high GC specific frequencies should have an excess of metal-poor GCs, because these galaxies will have captured (through accretion

or tidal stripping) proportionately larger numbers of metal-poor clusters in their outer regions. Similarly, FBG97 predict a trend in the sense that ellipticals with increasing specific frequency will have larger proportions of metal-poor GCs, and low-luminosity, low- S_N ellipticals should have relatively more metal-rich than metal-poor GCs. At least for the galaxies in our sample, we see the opposite behavior. The two cluster ellipticals with the highest S_N values show the same ratio of metal-rich to metal-poor GCs, and the same ratio exists in the S0 galaxy with moderate S_N . It is the lowest-luminosity, lowest- S_N galaxy in the sample, NGC 3379, that appears to have a larger proportion of blue GCs.

A hierarchical merging scenario may make more sense in terms of our results for the color distributions and relative proportions of red and blue GCs. In this type of picture, the massive cluster ellipticals might be expected to have a higher proportion of metal-rich GCs because they generally experience a larger number of the gas-rich major mergers over their histories than less massive galaxies do. As part of their simulations of hierarchical galaxy formation, Beasley et al. (2002) produce broadband color distributions for the GC systems of galaxies of different luminosities. The color distributions show a variety of morphologies, from distinctly bimodal (with either red or blue peaks dominating) to fairly flattened with only a small dip between the populations. A number of them appear at least qualitatively very much like our observed distributions, which likewise show a range in appearance and which presumably reflect their different evolutionary histories.

Color gradients.— NGC 4406 and NGC 4594 both exhibit small but significant (at $3\text{-}\sigma$ or better) gradients in their overall GC populations, in the sense that the ratio of blue to red GCs increases slightly with increasing galactocentric radius. This is in contrast to NGC 4472, which shows a weak color gradient in its inner regions but none in its overall population (Paper I). The $B - R$ versus radius data for NGC 3379 show a relatively steep gradient but the uncertainties are large (again possibly due to small-number statistics) and it is significant at only about the $2\text{-}\sigma$ level.

Color gradients in the GC systems of early-type galaxies are possible or expected in all the formation scenarios we are considering. In AZ92, FBG97, and the scenarios involving hierarchical merging, the blue, metal-poor GCs are expected to have a more extended distribution than the red GCs because the latter are younger and formed from gas that experienced subsequent dissipation. In the CMW98 model, the metal-poor GCs should be more extended relative to the metal-rich population, at least in giant ellipticals located near the centers of clusters, because large numbers of them are accreted into the galaxies' outer regions either through capture of dwarf galaxies or tidal stripping.

A specific prediction of FBG97 concerning color/metallicity gradients is that galaxies with larger specific frequencies should have steeper radial metallicity gradients, due to the greater numbers of metal-poor GCs at large radius. Our data appear to be inconsistent with this prediction, since NGC 4472, NGC 4406 and NGC 4594 show either no radial gradient or a very shallow one, and NGC 3379 appears to have the steepest color gradient of the sample.

It is worth noting that our measured color distributions and color gradients are global results and essentially cover the full radial extent of their GC systems. It is important to observationally test the models using these global properties since (as we saw in NGC 4472) color gradients can be present in the inner regions of galaxies but not there when one takes into account the entire system. Moreover, some of the models (e.g., CMW98, Santos 2003) make specific predictions with regard to GC populations in the outermost regions of ellipticals and good-quality, wide-field data are what is needed to address these.

Radial Distributions.— The best-fitting deVaucouleurs laws and power laws to the radial distributions of all three ellipticals in the sample have slopes that are the same within the errors (-1.6 for the deVaucouleurs law and -1.2 to -1.4 for the power law). The S0 galaxy NGC 4594 has the steepest slope (-2.1 for the deVaucouleurs law and -1.9 for the power law). The radial profiles for three of the four galaxies are better fit by deVaucouleurs laws than power laws, which typically overestimate the GC surface density by a larger amount in the outer regions of the profile. (For NGC 3379, the deVaucouleurs law and power law both provide good fits.)

Tidal stripping of GCs is thought to play a part in the evolution of the GC populations of galaxies in clusters, and is explicitly included in the FBG97 and CMW98 formation pictures. Our results for the GC radial distributions of two of the galaxies in the sample may have some significance with regard to tidal stripping and its role in the evolution of GC systems. NGC 3379 has the smallest apparent extent (~ 30 kpc) and the lowest S_N of the early-type sample. Since it is the largest galaxy in its environment, it is not likely to have lost a substantial number of its GCs due to tidal stripping. Thus its low specific frequency appears to be an intrinsic property of this galaxy. Finally, FBG97 predict that galaxies that have been tidally-stripped should have lower-than-average S_N values. However, the one galaxy in our sample that shows a hint that its GC system might be tidally truncated, NGC 4406, has a GC specific frequency that is almost identical to that of NGC 4472, which is a luminous giant elliptical located near the center of the Virgo cluster.

6. Summary

As part of a wide-field CCD survey of the GC populations of a sample of normal galaxies, we have investigated the GC system properties of the early-type galaxies NGC 3379, NGC 4406, and NGC 4594. Below is a summary of our findings.

1. The radial coverage of the data extends to $\sim 24\text{--}25'$, which corresponds to $\sim 70\text{--}100$ kpc at the distances of our targets. For all three galaxies, the GC surface density decreases until it is consistent with zero well before the end of the radial profile, strongly suggesting that we have observed the entire extent of the GC systems. The physical radius at which the GC surface density becomes consistent with zero ranges from 30 kpc for the least luminous elliptical to 80–100 kpc for the two more luminous galaxies.

2. The $B - R$ color distributions of the GCs of the target galaxies are better fit by a bimodal distribution than a unimodal one at $\geq 99.8\%$ confidence. The blue GC distributions are centered at $B - R \sim 1.1$ in all three galaxies; the metal-rich populations are centered between $B - R \sim 1.3$ and 1.5. The two more luminous galaxies, NGC 4406 and NGC 4594, have $\sim 60\%$ blue and $\sim 40\%$ red GCs. NGC 4472 shows similar proportions (Paper I). In the lower-luminosity elliptical, NGC 3379, blue GCs make up $\sim 70\%$ of the total population.

3. All three galaxies presented here show modest negative color gradients in their GC systems, caused by the increasing ratio of blue to red GCs with increasing projected radial distance.

4. S_N for NGC 4406's GC population is 3.5 ± 0.5 , which represents a $\sim 20\%$ reduction in the number of GCs compared to previous estimates. We obtained a similar result for the other giant Virgo elliptical in the sample, NGC 4472 (Paper I). NGC 3379 and NGC 4594 have S_N of 1.2 ± 0.3 and 2.1 ± 0.3 , respectively; these values are similar to those from past studies but have much smaller errors.

5. The mass-normalized numbers of blue, metal-poor GCs (T_{blue}) in the Virgo cluster ellipticals are almost identical and are ~ 2.5 times larger than the value for the field elliptical NGC 3379, whose blue GC population is comparable to that of spirals of similar mass. The field S0 NGC 4594 has T_{blue} between that of NGC 3379 and the cluster ellipticals. To date, our survey data suggest that merging the blue GC populations of typical spirals is not likely to produce enough metal-poor GCs to account for the blue populations in luminous, high- S_N cluster ellipticals; however, it may be able to account for the blue GC populations of ellipticals of more moderate luminosity. The proportion of blue GCs is roughly constant for three of the galaxies in the early-type sample, and slightly larger for the galaxy with the lowest specific frequency. This result is not consistent with galaxy formation models (e.g., FBG97 and CMW98) that predict that galaxies with larger S_N should have proportionately more metal-poor GCs.

6. We compare our results with the predictions and assumptions of a number of models for the formation of massive galaxies and their GC systems. The general scenario that appears most consistent with the observations is one in which metal-poor GCs form in the early Universe in merging protogalactic building blocks. Subsequent hierarchical merging produces metal-rich GCs and eventually results in today's massive galaxies. Detailed models within this hierarchical framework are currently being produced and our data on the global properties of massive galaxies' GC systems are likely to prove valuable for helping to constrain and test the theoretical work in this area.

K.L.R. gratefully acknowledges financial support from a NASA Graduate Student Researchers Fellowship for this project. S.E.Z. acknowledges support for this work from the Michigan State University Foundation and NASA Long-Term Space Astrophysics Grant NAG5-11319. We thank Arunav Kundu and John Salzer for obtaining post-calibration data at the WIYN telescope in 2001 April and 2002 March, respectively. We have benefited from discussions with Kathryn Johnston

and Brad Whitmore, which resulted in improvements to the paper. We also thank the referee, Terry Bridges, for providing valuable suggestions and comments on the manuscript. Finally, we are grateful to the staff at Kitt Peak National Observatory and WIYN for assistance during the observing runs. This research has made use of the NASA/IPAC Extragalactic Database (NED), which is operated by the Jet Propulsion Laboratory, California Institute of Technology, under contract with the National Aeronautics and Space Administration.

REFERENCES

- Ashman, K.M., Bird, C.M., & Zepf, S.E. 1994, *AJ*, 108, 2348
- Ashman, K.M., & Zepf, S.E. 1992, *ApJ*, 384, 50
- Ashman, K.M., & Zepf, S.E. 1998, *Globular Cluster Systems* (Cambridge: Cambridge University Press)
- Baum, W.A. 1955, *PASP*, 67, 328
- Beasley, M.A., Baugh, C.M., Forbes, D.A., Sharples, R.M., & Frenk, C.S. 2002, *MNRAS*, 333, 383
- Bridges, T.J. & Hanes, D.A. 1992, *AJ*, 103, 800
- Cohen, J.G. 1988, *AJ*, 95, 682
- Côté, P., Marzke, R.O., & West, M.J. 1998, *ApJ*, 501, 554
- de Vaucouleurs, G., de Vaucouleurs, A., Corwin Jr., H.G., Buta, R.J., Paturel, G., & Fouque, P. 1991, *Third Reference Catalogue of Bright Galaxies* (New York: Springer)
- Dressler, A., Lynden-Bell, D., Burstein, D., Davies, R.L., Faber, S.M., Terlevich, R.J., & Wegner, G. 1987, *ApJ*, 313, 42
- Faber, S.M., Dressler, A., Davies, R.L., Burstein, D., & Lynden-Bell, D. 1987, in *Nearly Normal Galaxies: From the Planck Time to the Present* (New York: Springer-Verlag)
- Forbes, D.A., Brodie, J.P., & Grillmair, C.J. 1997a, *AJ*, 113, 1652
- Forbes, D.A., Grillmair, C.J., & Smith, R.C. 1997b, *AJ*, 113, 1648
- Gebhardt, K. & Kissler-Patig, M. 1999, *AJ*, 118, 1526
- Geisler, D., Lee, M.G., & Kim, E. 1996, *AJ*, 111, 1529
- Harris, W.E. 1991, *ARA&A*, 29, 543
- Harris, W.E. & van den Bergh, S. 1981, *AJ*, 86, 1627
- Kormendy, J. & Djorgovski, S. 1989, *ARA&A*, 27, 235
- Kundu, A. & Whitmore, B.C. 2001, *AJ*, 121, 2950
- Kundu, A., Whitmore, B.C., Sparks, W.B., & Macchetto, F.D. 1999, *ApJ*, 513, 733
- Landolt, A.U. 1992, *AJ*, 104, 340
- Larsen, S.S., Brodie, J.P., Huchra, J.P., Forbes, D.A., & Grillmair, C.J. 2001, *AJ*, 121, 2974

- Mendez, R.A., Platais, I., Girard, T.M., Kozhurina-Platais, V., & van Altena, W.F. 2000, *AJ*, 119, 813
- Mendez, R.A. & van Altena, W.F. 1996, *AJ*, 112, 655
- Pahre, M.A., Djorgovski, S.G., & de Carvalho, R.R. 1995, *ApJ*, 453, L17
- Rhode, K.L. & Zepf, S.E. 2001, *AJ*, 121, 210
- Rhode, K.L. & Zepf, S.E. 2003, *AJ*, in press
- Sandage, A. 1961, “The Hubble Atlas of Galaxies” (Washington, D.C.: Carnegie Institution of Washington)
- Santos, M.R. 2003, in *Extragalactic Globular Cluster Systems*, ed. M. Kissler-Patig (New York: Springer-Verlag)
- Schlegel, D.J., Finkbeiner, D.P., & Davis, M. 1998, *ApJ*, 500, 525
- Tonry, J.L., Blakeslee, J.P., Ajhar, E.A., Fletcher, A.B., Luppino, G.A., Metzger, M.R., & Moore, C.B. 2001, *ApJ*, 546, 681
- Whitmore, B.C. & Schweizer, F. 1995, *AJ*, 109, 960
- Whitmore, B.C., Schweizer, F., Leitherer, C., Borne, K., & Robert, C. 1993, *AJ*, 106, 1354
- Whitmore, B.C., Sparks, W.B., Lucas, R.A., Macchetto, F.D., & Biretta, J.A. 1995, *ApJ*, 454, L73
- Zepf, S.E., & Ashman, K.M. 1993, *MNRAS*, 264, 611
- Zepf, S.E. & Silk, J. 1996, *ApJ*, 466, 114

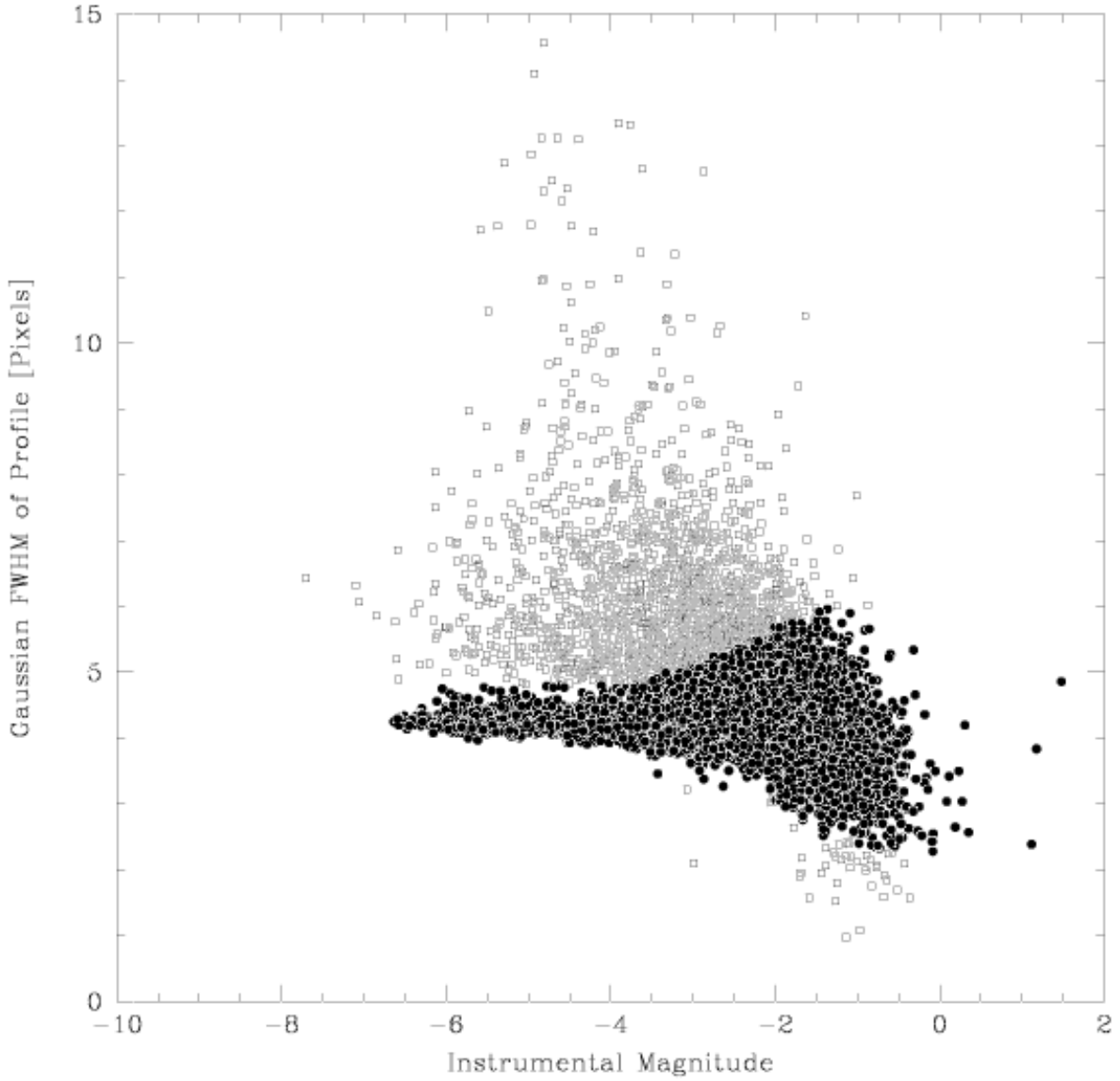


Fig. 1.— Gaussian FWHM of the radial profile versus instrumental magnitude for 8053 objects in the stacked Mosaic *V* image of NGC 4594. Open circles are objects that are deemed extended and that were subsequently eliminated from the list of GC candidates. Filled circles mark the objects that were accepted as possible point sources.

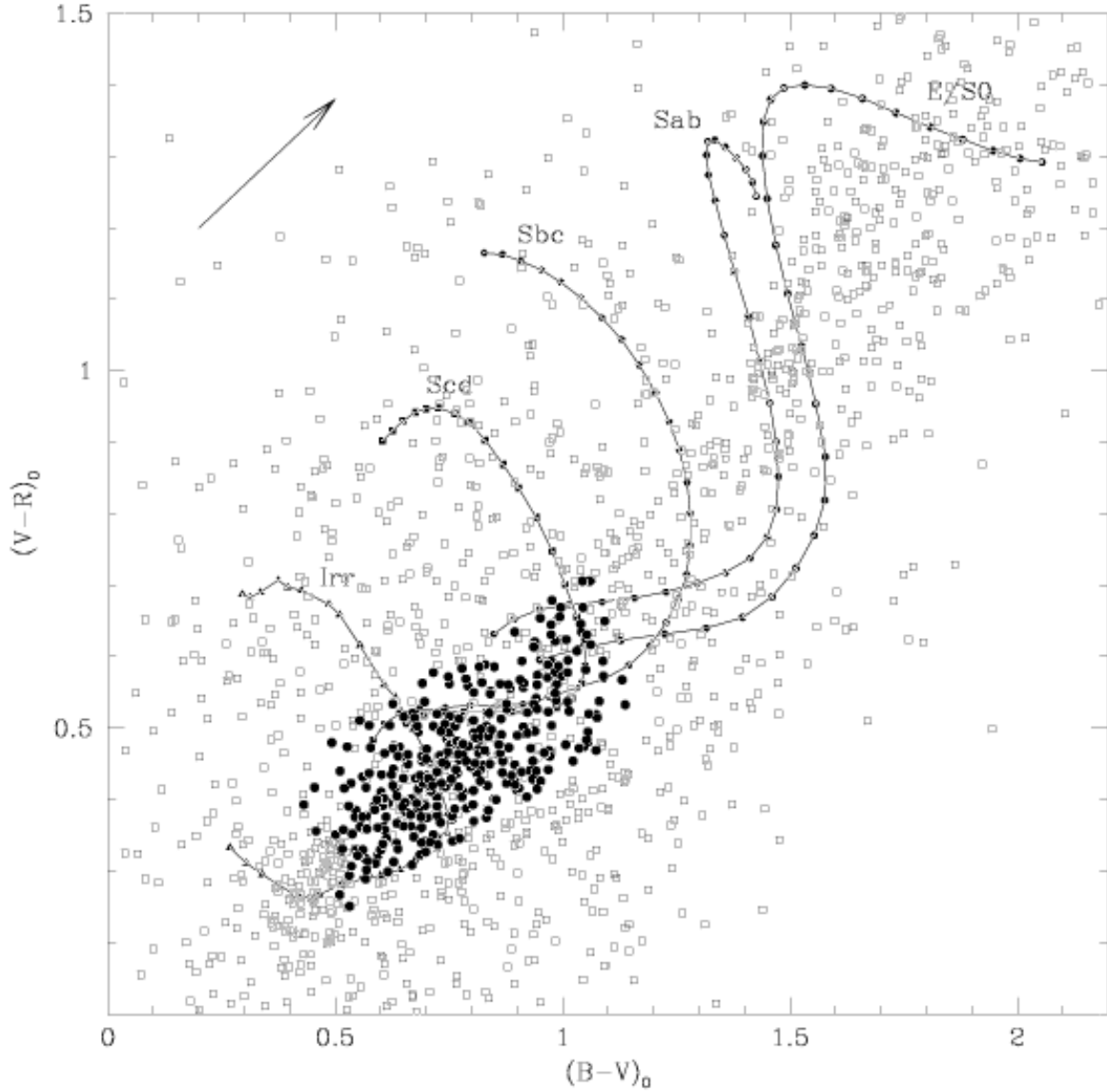


Fig. 2.— Color selection of GC candidates in NGC 3379. Open squares are 1728 unresolved objects in the Mosaic images and filled circles are the final set of 321 GC candidates around NGC 3379. For reference, the locations in the BVR plane of galaxies of various types are shown as tracks the galaxies would follow with increasing redshift. See Paper I for details on how the tracks were produced. A reddening vector of length $A_V = 1$ mag appears in the upper left corner.

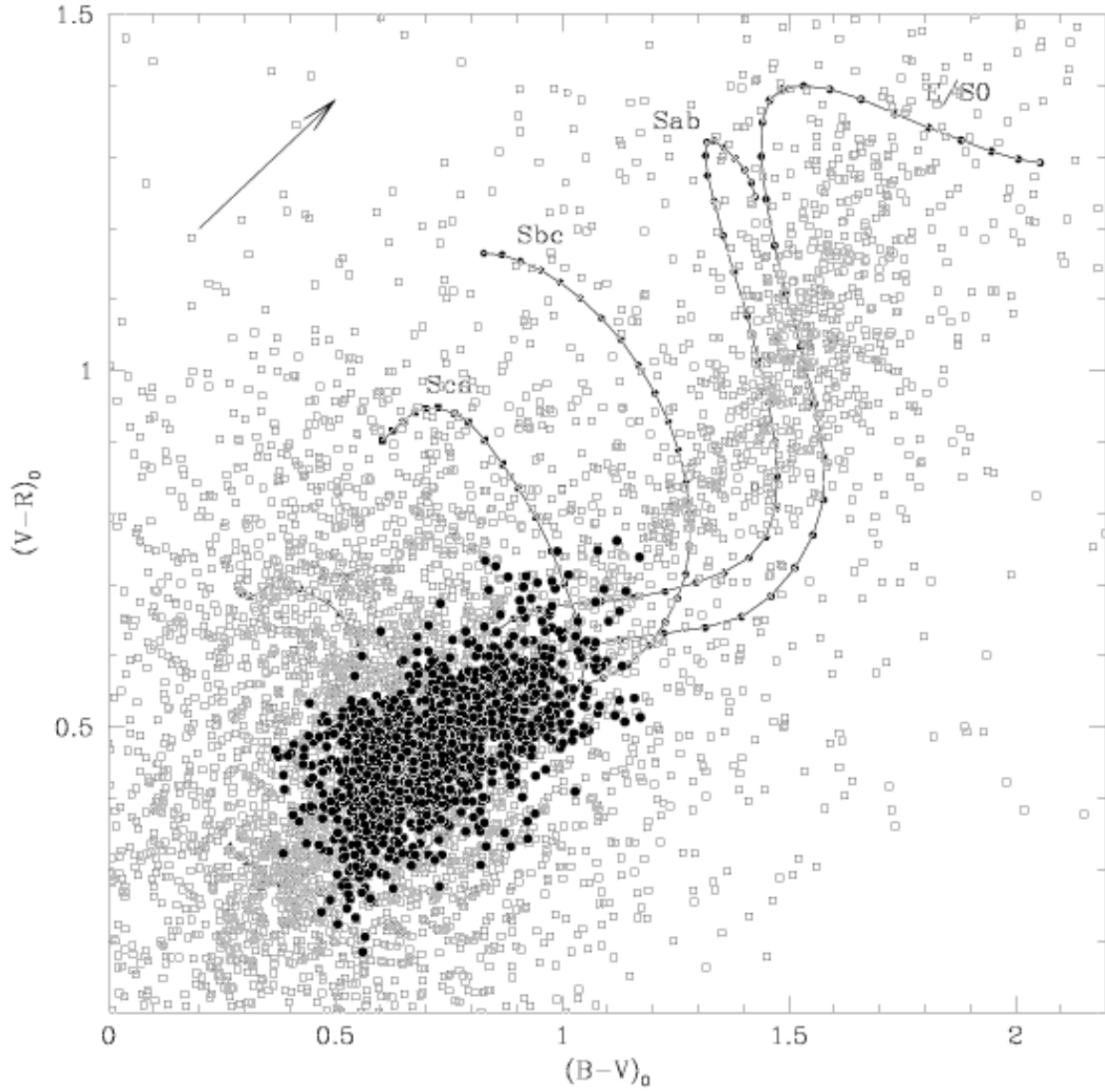


Fig. 3.— Color selection of GC candidates in NGC 4406. Open squares are 6604 unresolved objects in the Mosaic images and filled circles are the final set of 1400 GC candidates.

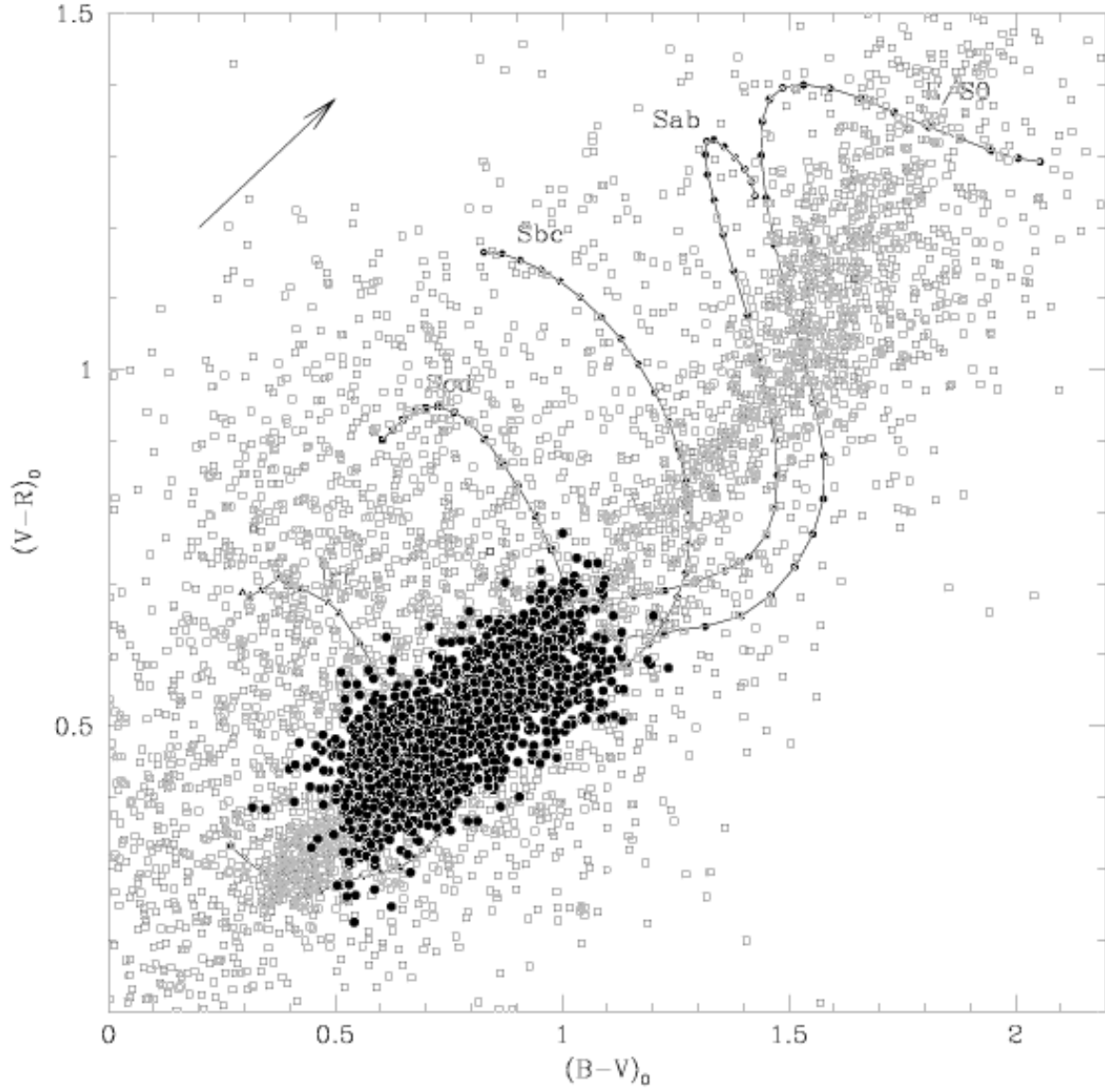


Fig. 4.— Color selection of GC candidates in NGC 4594. Open squares are 5708 objects that passed the extended source cut and filled circles are the final set of 1748 GC candidates.

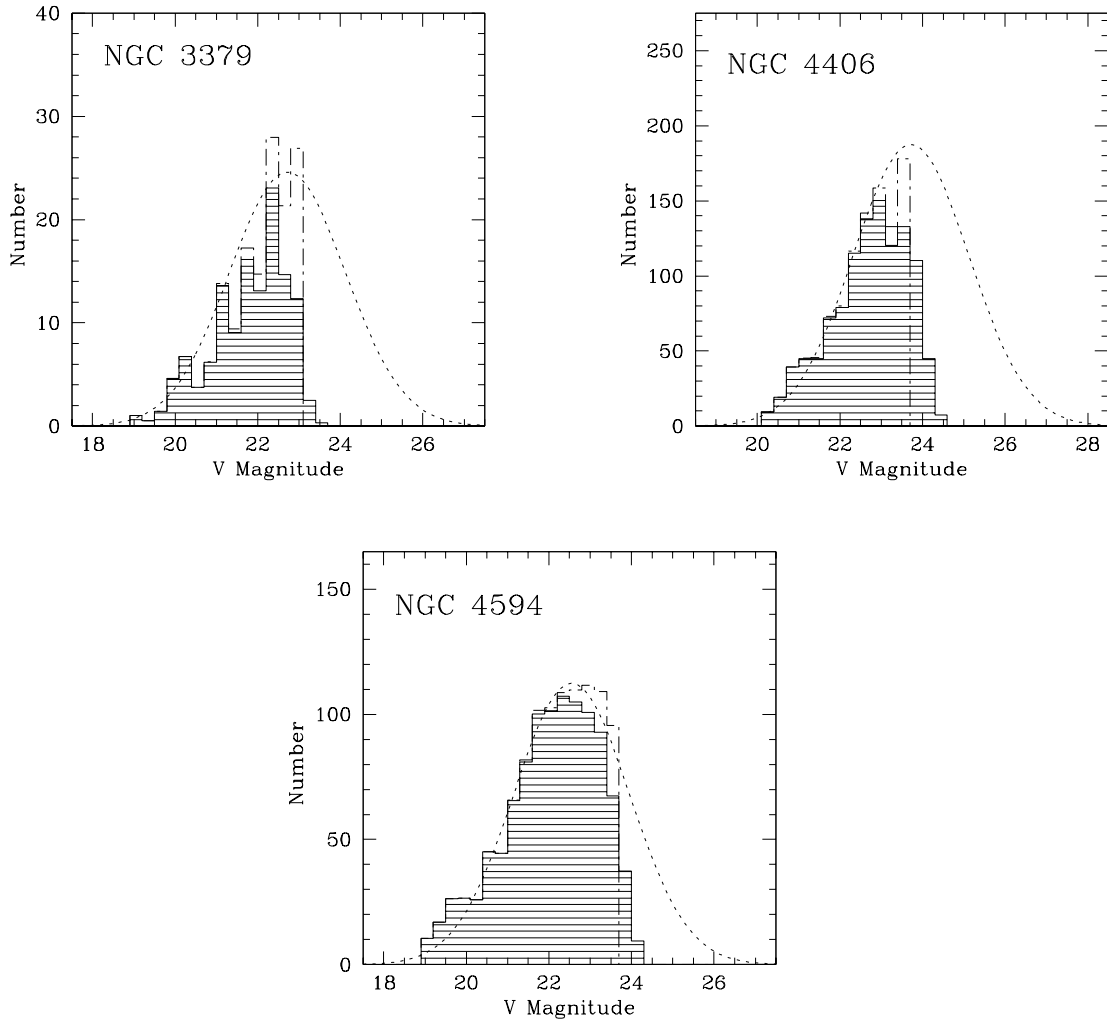


Fig. 5.— GCLF fitting for the three galaxies. The shaded histogram is the observed GC luminosity function. The dashed line shows the completeness-corrected data used in the fit (i.e., bins with completeness $>45\%$). The dotted line is the best-fit Gaussian distribution.

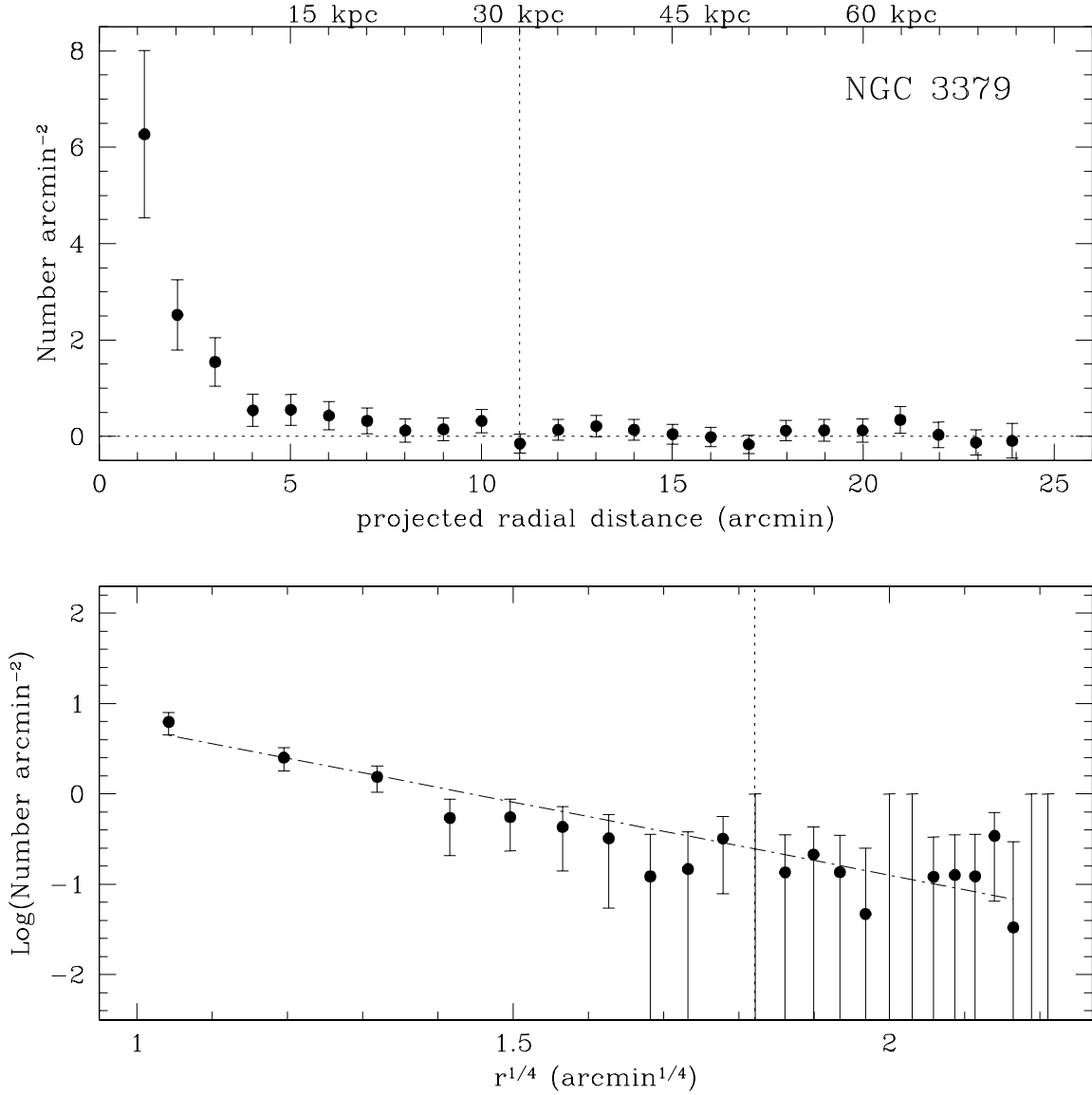


Fig. 6.— Radial distribution of GCs in NGC 3379, plotted as surface density vs. projected radial distance (top) and as the log of the surface density vs. $r^{1/4}$ (bottom). The dotted line in the top plot indicates zero surface density and the dashed line in the bottom plot is the best-fit deVaucouleurs law. The vertical line in both plots marks the location where the surface density is consistent with zero within the errors. The data have been corrected for contamination, missing spatial coverage, and magnitude incompleteness.

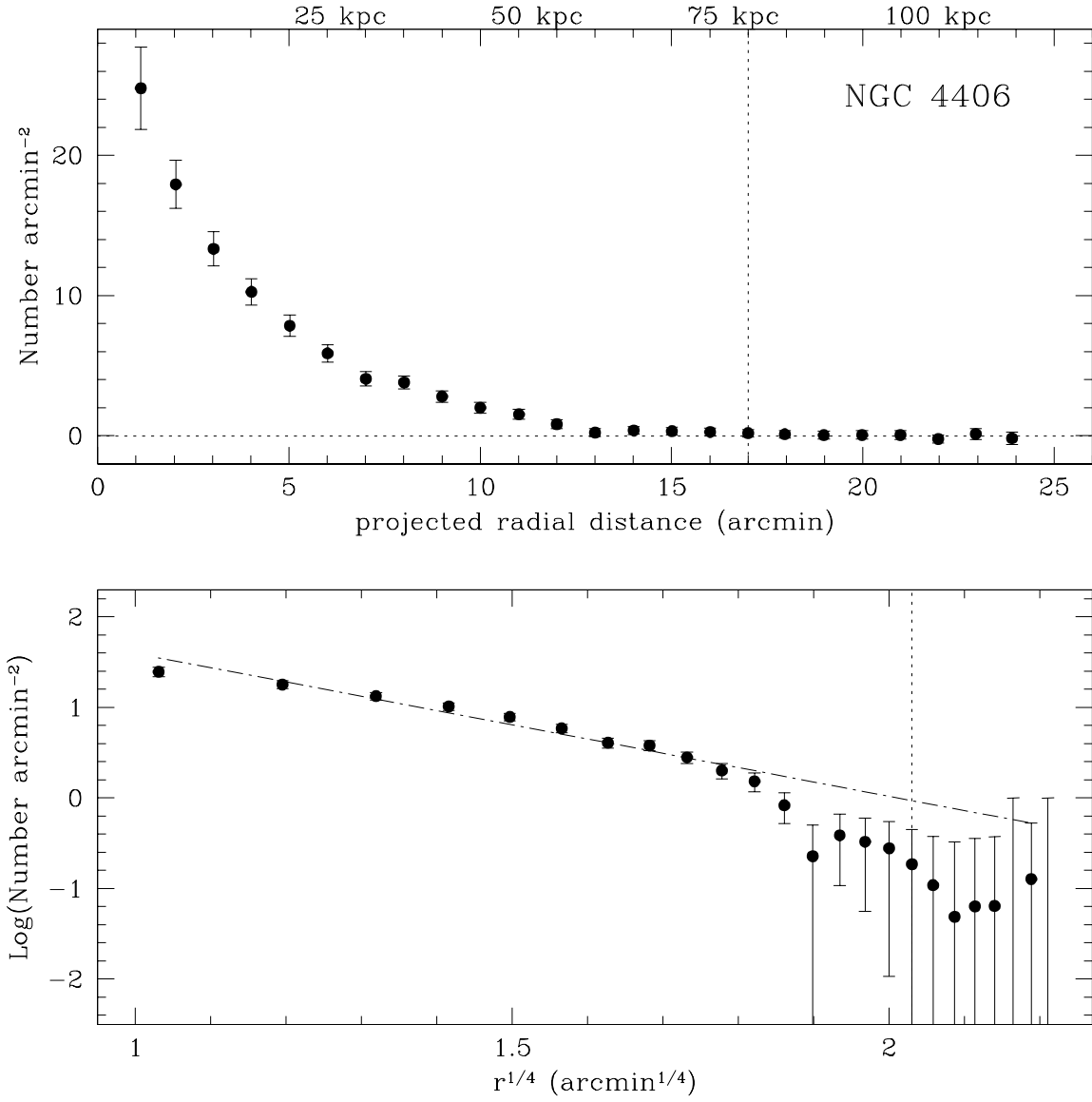


Fig. 7.— Radial distribution of GCs in NGC 4406, plotted in the same way as in Figure 6.

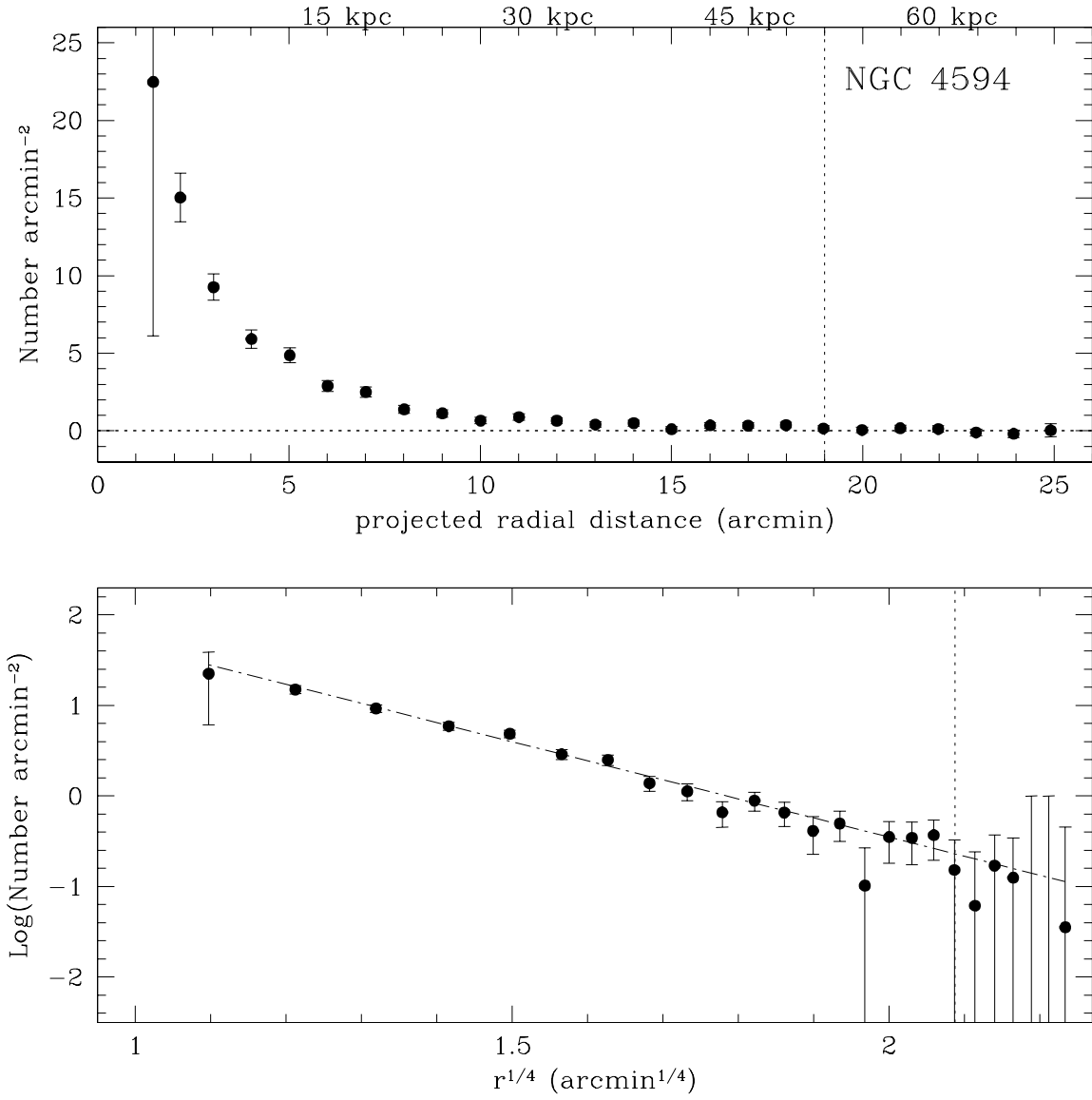


Fig. 8.— Radial distribution of GCs in NGC 4594, plotted in the same way as in Figure 6.

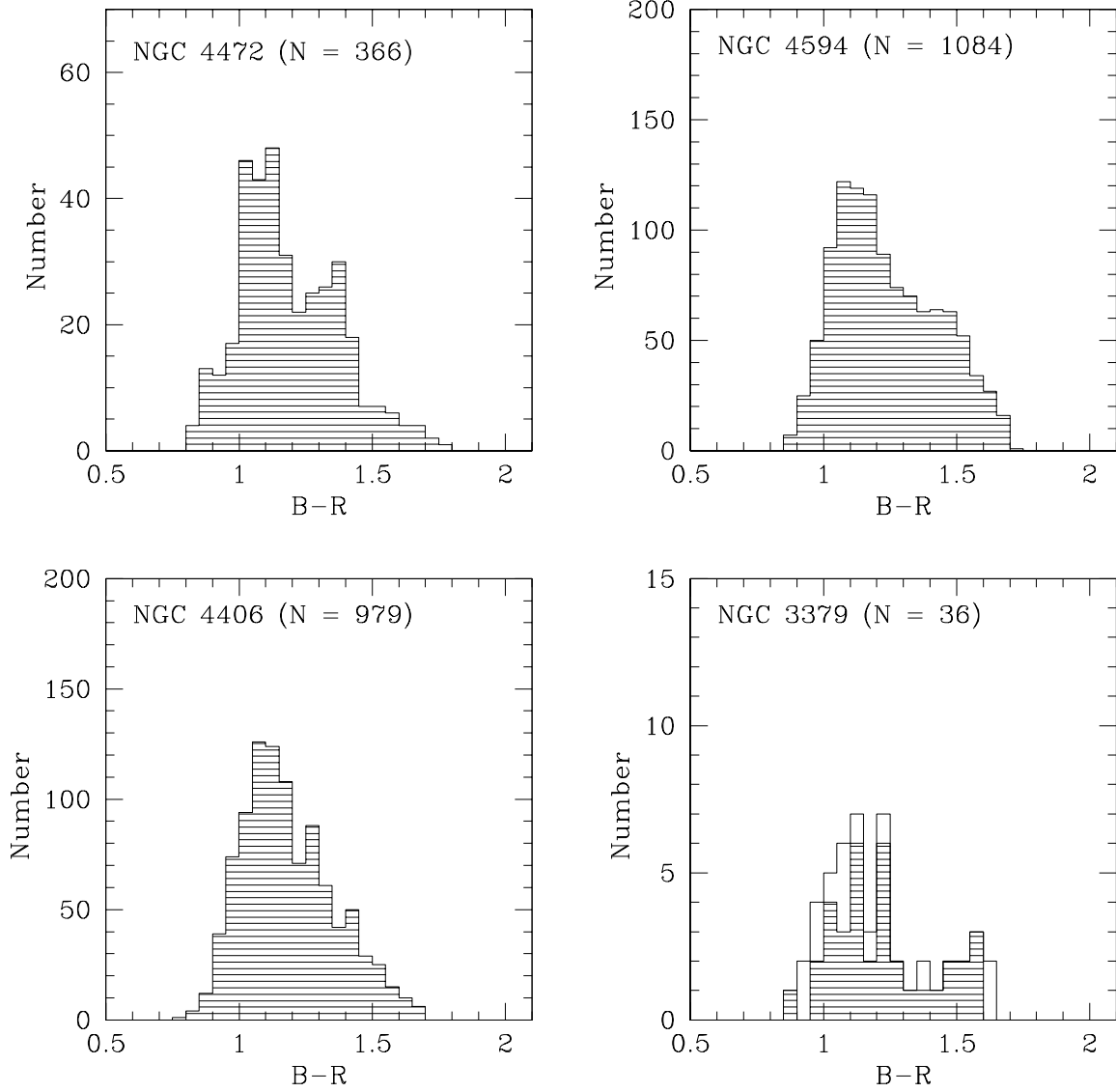


Fig. 9.— $B - R$ distributions for the early-type galaxy sample, including NGC 4472 from Paper I. For NGC 3379, the 36-object sample used to estimate the blue/red GC proportions is shown as a shaded histogram and the 50-object sample used as input to KMM is plotted with a solid line.

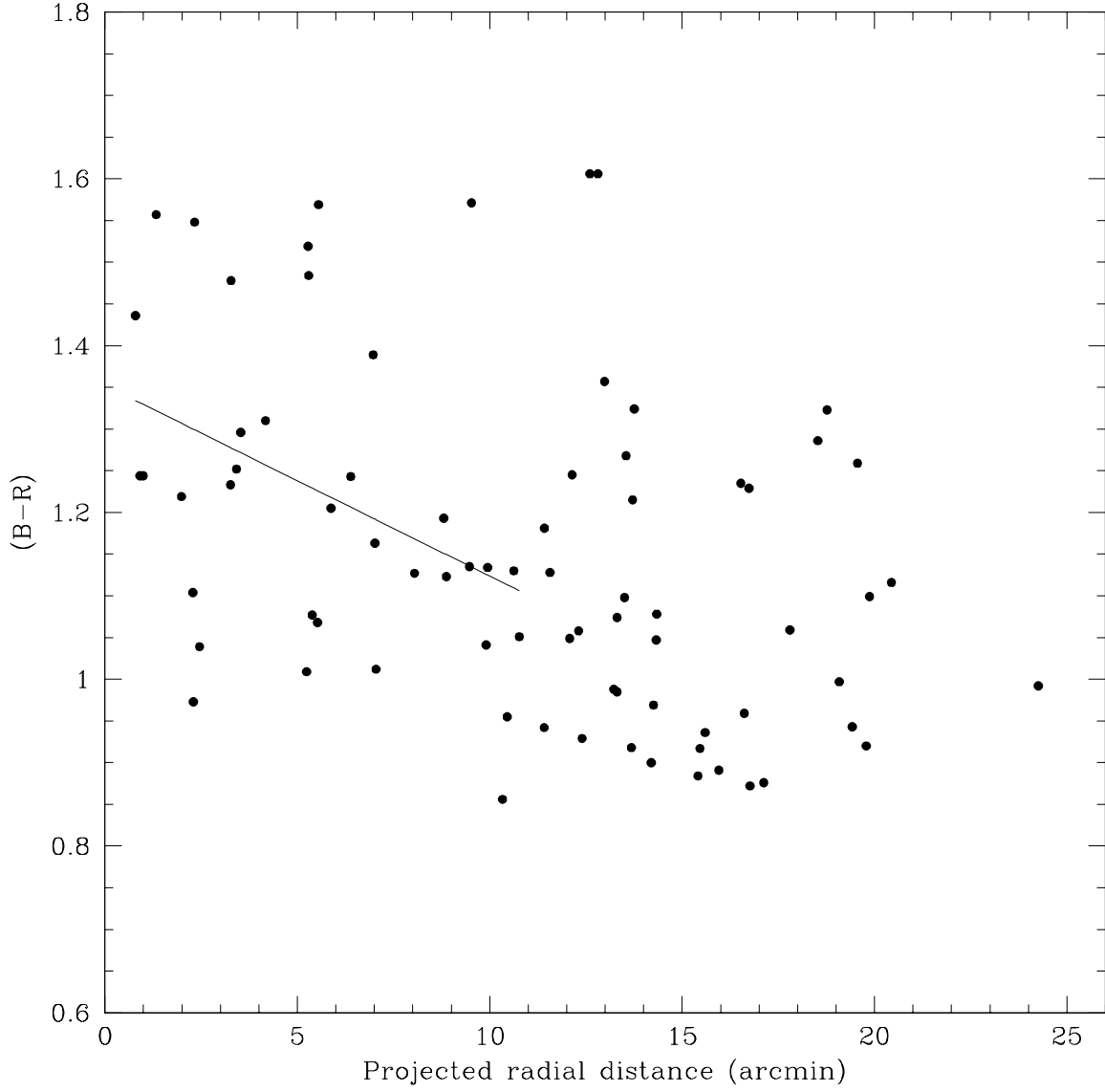


Fig. 10.— $B - R$ color versus projected radial distance of the 90% sample of GC candidates in NGC 3379. The solid line is a linear fit to the data inside $11'$; its slope is -0.023 ± 0.010 .

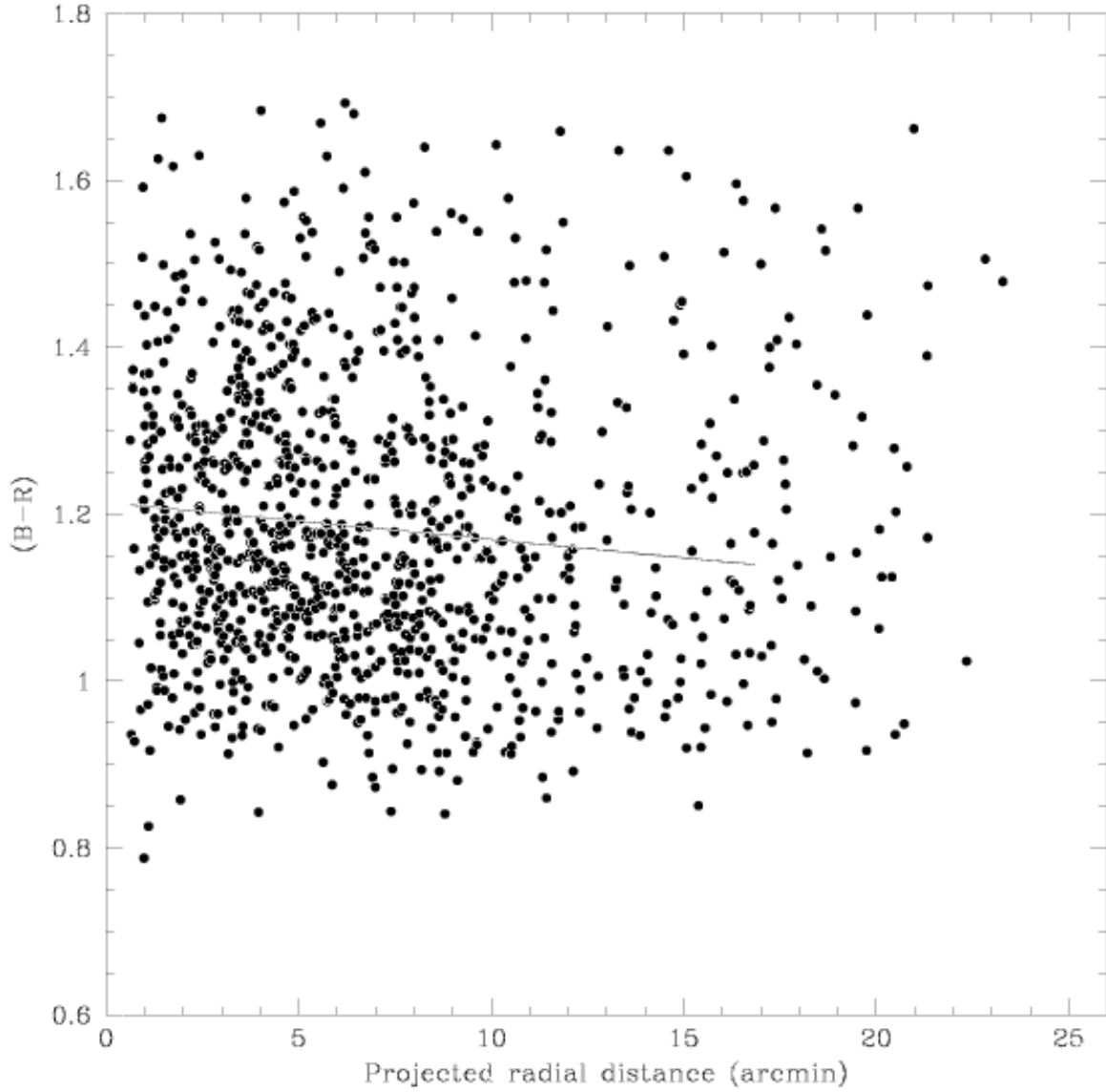


Fig. 11.— $B - R$ color versus projected radial distance of the 90% sample of GC candidates in NGC 4406. The solid line is a linear fit to the data inside $17'$, with a slope of -0.004 ± 0.001 .

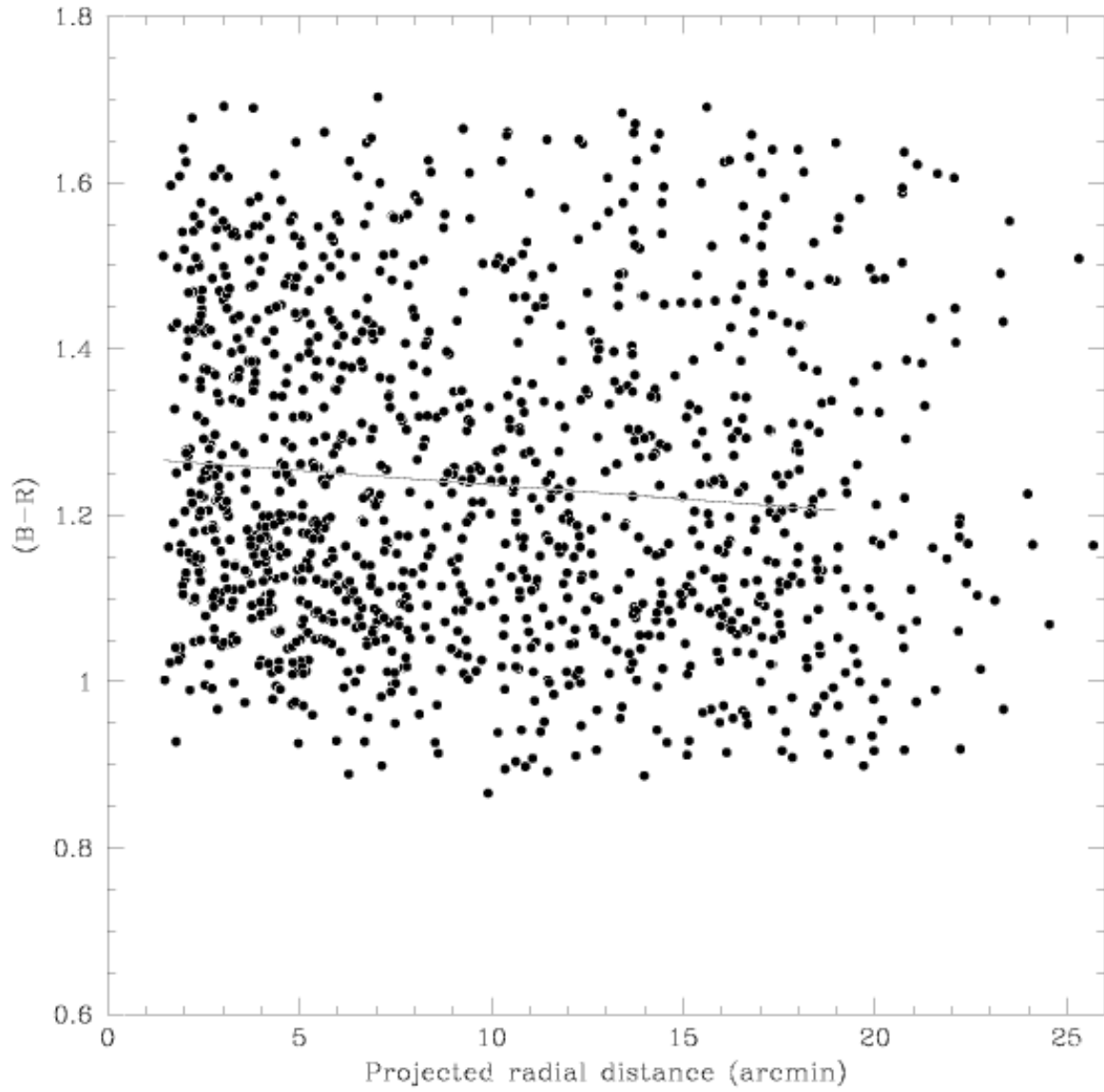


Fig. 12.— $B - R$ color versus projected radial distance of the 90% sample of GC candidates in NGC 4594. The solid line is a linear fit to the data inside $19'$, with a slope of -0.003 ± 0.001 .

Table 1. Basic Properties of Galaxies in the Early-type Sample

Name	Type	$m - M$	Dist (Mpc)	M_V^T	Environment
NGC4472 (M49)	E2	31.12	16.7	−23.1	Virgo cluster
NGC4406 (M86)	E3	31.12	16.7	−22.3	Virgo cluster
NGC3379 (M105)	E1	30.12	10.6	−20.9	Leo-I group
NGC4594 (M104)	S0	29.95	9.8	−22.4	Field

Note. — Virgo cluster distance is from Whitmore et al. (1995) (HST observations of M87’s GCLF); other distances are from Tonry et al. (2001) (surface brightness fluctuations). Magnitude for NGC 4472 from Rhode & Zepf (2001); all others from combining V_T^0 from RC3 (deVaucouleurs et al. 1991) with $m - M$.

Table 2. Aperture Corrections Used for Photometry of Mosaic Sources

	NGC 3379	NGC 4406	NGC 4594
B	-0.149 ± 0.003	-0.167 ± 0.005	-0.138 ± 0.002
V	-0.171 ± 0.004	-0.224 ± 0.006	-0.262 ± 0.004
R	-0.237 ± 0.006	-0.159 ± 0.005	-0.202 ± 0.004

Table 3. Extinction Corrections Used for Photometry of Mosaic Sources

	NGC 3379	NGC 4406	NGC 4594
A_B	0.105	0.126	0.222
A_V	0.081	0.097	0.171
A_R	0.065	0.077	0.138

Table 4. 50% Completeness Limits of Mosaic Images

	NGC 3379	NGC 4406	NGC 4594
<i>B</i>	23.56	25.44	24.63
<i>V</i>	24.09	24.17	23.98
<i>R</i>	23.40	23.48	23.64

Table 5. HST WFPC2 Observations Analyzed for this Study

Proposal ID	Target Name	PI	Ang Sep ($^{\circ}$)	Filter
NGC 3379:				
5512	NGC 3379-Nuc1	Faber	0.5	F814W
7909	Any	Casertano	3.0	F606W
8059	List-2	Casertano	5.2	F606W
5233	NGC 3379-Pos3	Westpfahl	6.2	F814W
5512	NGC 3384	Faber	6.9	F814W
NGC 4406:				
5512	NGC 4406	Faber	0.4	F814W
7377	VCC 896	Miller	9.4	F555W
7909	Any	Casertano	10.0	F606W
7202	Parallel Field	Windhorst	10.1	F814W
7566	NGC 4374	Green	13.5	F606W
NGC 4594:				
5512	NGC 4594-Nuc1	Faber	0.5	F814W
5091	Parallel Field	Groth	4.5	F814W
5369	Hi Lat	Griffiths	8.2	F814W

Table 6. Corrected Radial Profiles of GCs in Target Galaxies

NGC 3379			NGC 4406			NGC 4594		
r ($'$)	σ (arcmin^{-2})	Cvg	r ($'$)	σ (arcmin^{-2})	Cvg	r ($'$)	σ (arcmin^{-2})	Cvg
1.2....	6.27 ± 1.73	0.77	1.1....	24.79 ± 2.95	0.92	1.4....	22.48 ± 16.36	0.02
2.0....	2.52 ± 0.73	1.00	2.0....	17.94 ± 1.72	1.00	2.2....	15.03 ± 1.57	0.61
3.0....	1.54 ± 0.50	1.00	3.0....	13.34 ± 1.22	1.00	3.0....	9.26 ± 0.85	0.90
4.0....	0.54 ± 0.34	1.00	4.0....	10.26 ± 0.95	1.00	4.0....	5.92 ± 0.58	0.98
5.0....	0.55 ± 0.32	0.93	5.0....	7.85 ± 0.76	1.00	5.0....	4.87 ± 0.48	1.00
6.0....	0.43 ± 0.29	0.89	6.0....	5.88 ± 0.62	1.00	6.0....	2.89 ± 0.36	1.00
7.0....	0.32 ± 0.27	0.88	7.0....	4.07 ± 0.51	1.00	7.0....	2.50 ± 0.33	0.97
8.0....	0.12 ± 0.24	0.89	8.0....	3.81 ± 0.47	1.00	8.0....	1.38 ± 0.26	0.98
9.0....	0.15 ± 0.23	0.90	9.0....	2.81 ± 0.41	0.99	9.0....	1.13 ± 0.24	0.99
10.0....	0.32 ± 0.24	0.90	10.0....	2.01 ± 0.39	0.81	10.0....	0.66 ± 0.21	0.98
11.0....	-0.15 ± 0.20	0.96	11.0....	1.53 ± 0.35	0.80	11.0....	0.89 ± 0.21	1.00
12.0....	0.14 ± 0.22	0.95	12.0....	0.83 ± 0.31	0.78	12.0....	0.66 ± 0.20	0.98
13.0....	0.21 ± 0.22	0.94	13.0....	0.23 ± 0.27	0.75	13.0....	0.41 ± 0.18	0.96
14.0....	0.14 ± 0.21	0.91	14.0....	0.39 ± 0.28	0.75	14.0....	0.50 ± 0.18	0.99
15.0....	0.05 ± 0.21	0.91	15.0....	0.33 ± 0.27	0.74	15.0....	0.10 ± 0.16	0.99
16.0....	-0.01 ± 0.20	0.93	16.0....	0.28 ± 0.27	0.74	16.0....	0.35 ± 0.17	0.98
17.0....	-0.16 ± 0.19	0.92	17.0....	0.19 ± 0.26	0.74	17.0....	0.34 ± 0.17	0.98
18.0....	0.12 ± 0.21	0.69	18.0....	0.11 ± 0.27	0.54	18.0....	0.37 ± 0.17	0.85
19.0....	0.13 ± 0.23	0.47	19.0....	0.05 ± 0.28	0.36	19.0....	0.15 ± 0.17	0.63
20.0....	0.12 ± 0.24	0.36	20.0....	0.06 ± 0.29	0.26	20.0....	0.06 ± 0.18	0.45
21.0....	0.34 ± 0.28	0.26	21.0....	0.06 ± 0.31	0.20	21.0....	0.17 ± 0.20	0.32
22.0....	0.03 ± 0.26	0.18	22.0....	-0.22 ± 0.29	0.14	22.0....	0.13 ± 0.22	0.23
22.9....	-0.13 ± 0.26	0.11	22.9....	0.13 ± 0.40	0.08	23.0....	-0.10 ± 0.22	0.15
23.9....	-0.09 ± 0.36	0.04	23.9....	-0.17 ± 0.43	0.04	23.9....	-0.19 ± 0.25	0.09
						24.9....	0.04 ± 0.42	0.03

Note. — A subtractive correction for contamination has been applied to the data, resulting in negative surface densities in some of the outer bins.

Table 7. Coefficients from Fitting Radial Profile Data

Galaxy	deVaucouleurs Law		Power Law	
	a0	a1	a0	a1
NGC 3379	2.33 ± 0.22	-1.62 ± 0.15	0.83 ± 0.09	-1.41 ± 0.13
NGC 4406	3.18 ± 0.09	-1.58 ± 0.06	1.66 ± 0.04	-1.24 ± 0.05
NGC 4594	3.76 ± 0.11	-2.11 ± 0.08	1.87 ± 0.05	-1.85 ± 0.07

Table 8. Total Numbers and Specific Frequencies for Galaxies in the Early-type Sample

Name	M_V^T	N_{GC}	S_N	Extent (kpc)	T	T_{blue}	Prev S_N^\dagger	Ref
NGC4472	-23.1	5900	3.6 ± 0.6	100	4.2	2.6	4.5 ± 1.3	1
NGC4406	-22.3	2900	3.5 ± 0.5	80	4.1	2.5	4.6 ± 1.1	1
NGC3379	-20.9	270	1.2 ± 0.3	30	1.4	1.0	1.1 ± 0.6	1
NGC4594	-22.4	1900	2.1 ± 0.3	50	3.2	2.0	2 ± 1	2

References. — (1) Harris (1991); (2) Bridges & Hanes (1992)

[†]The S_N values given in this column were calculated by combining N_{GC} from the previous study with the galaxy magnitude listed in column (2).